## **Exploring the Bottlenecks of Anionic Redox in Li-rich Layered Sulfides**

1 2

- 3 Sujoy Saha<sup>1,2,3†</sup>, Gaurav Assat<sup>1,2,3†</sup>, Moulay Tahar Sougrati<sup>3,4,5</sup>, Dominique Foix<sup>3,6</sup>, Haifeng Li<sup>7</sup>, Jean
- 4 Vergnet<sup>1,3</sup>, Soma Turi<sup>1</sup>, Yang Ha<sup>8</sup>, Wanli Yang<sup>8</sup>, Jordi Cabana<sup>7</sup>, Gwenaëlle Rousse<sup>1,2,3</sup>, Artem M. Abakumov<sup>9</sup>,
- 5 Jean-Marie Tarascon<sup>1,2,3</sup>\*

6

- 7 ¹Collège de France, Chaire de Chimie du Solide et de l'Energie, UMR 8260, 11 Place Marcelin Berthelot, 75231 CEDEX
- 8 05 Paris, France
- 9 <sup>2</sup>Sorbonne Université, 4 Place Jussieu, F-75005 Paris, France
- <sup>3</sup>Réseau sur le Stockage Electrochimique de l'Energie (RS2E), FR CNRS 3459, 33 Rue Saint Leu, 80039 Amiens, France
- <sup>4</sup>Institut Charles Gerhardt UMR 5253, 34095 Montpellier Cedex 5, France
- 12 <sup>5</sup>ALISTORE-European Research Institute, 33 rue Saint-Leu, 80039 Amiens Cedex, France
- 13 <sup>6</sup>IPREM/ECP (UMR 5254), Université de Pau, 2 Avenue Pierre Angot, 64053 Pau Cedex 9, France
- <sup>7</sup>Department of Chemistry, University of Illinois at Chicago, Chicago, Illinois 60607, United States
- 15 \*Advanced Light Source, Lawrence Berkeley National Laboratory, One Cyclotron Road, Berkeley, CA 94720, USA
- <sup>9</sup>Center for Energy Science and Technology, Skolkovo Institute of Science and Technology, Nobel Str. 3, 143026
- 17 Moscow, Russia
- <sup>†</sup> These authors contributed equally to this work.
- \*e-mail: jean-marie.tarascon@college-de-france.fr

20

21

22

23 24

25

26

27

28

29

30

31 32

33

34

35

36

### **Abstract**

To satisfy the long-awaited need of new lithium-ion battery cathode materials with higher energy density, anionic redox chemistry has emerged as a new paradigm that is responsible for the high capacity in Li-rich layered oxides, for example, in Li<sub>1.2</sub>Ni<sub>0.13</sub>Mn<sub>0.54</sub>Co<sub>0.13</sub>O<sub>2</sub> (Li-rich NMC). However, their marketimplementation has been plagued by certain bottlenecks originating intriguingly from the anionic redox activity itself. To fundamentally understand these bottlenecks (voltage fade, hysteresis and sluggish kinetics), we decided to target the ligand by switching to isostructural Li-rich layered sulfides. Herein, we designed new Li<sub>1.33-2y/3</sub>Ti<sub>0.67-y/3</sub>Fe<sub>y</sub>S<sub>2</sub> cathodes that enlist sustained reversible capacities of ~245 mAh·g<sup>-1</sup> due to cumulated cationic (Fe<sup>2+/3+</sup>) and anionic (S<sup>2-</sup> / S<sup>n-</sup>, n < 2) redox processes. In-depth electrochemical analysis revealed nearly zero irreversible capacity during the initial cycle, very small voltage fade upon long cycling, with low voltage hysteresis and fast kinetics, which contrasts positively with respect to their Li-rich NMC oxide analogues. Our study, further complemented with DFT calculations, demonstrates that moving from oxygen to sulfur as the ligand is an adequate strategy to partially mitigate the practical bottlenecks affecting anionic redox, although with an expected penalty in cell voltage. Altogether the present findings provide chemical clues on improving the holistic performance of anionic redox electrodes via ligand tuning, and hence strengthen the feasibility to ultimately capitalize on the energy benefits of oxygen redox.

#### Introduction

37

38

39

40

41 42

43 44

45 46

47

48 49

50

51

52

53 54

55

56

57

58 59

60

61

62 63

64

65

66

67

68

69 70

71

72

73

74

75

76 77

78

79

Over the past three decades, Li-ion batteries (LIB) have revolutionized the portable electronics industry, while more recently reorienting the automotive industry by enabling electric vehicles. <sup>1,2</sup> To comply with the ever-growing demands of energy for such applications, increasing the energy density of LIBs has become a formidable challenge. For many years, the cathode materials in LIBs relied solely on the transition metal (cationic) redox, until the recently discovered anionic redox, i.e., electrochemical participation of the oxygen ligands, became a new approach for designing higher energy cathode materials. Li-rich Mn-based layered oxides, for example, Li<sub>1.2</sub>Ni<sub>0.2</sub>Mn<sub>0.6</sub>O<sub>2</sub> and Li<sub>1.2</sub>Ni<sub>0.13</sub>Mn<sub>0.54</sub>Co<sub>0.13</sub>O<sub>2</sub> (Li-rich NMC) hold the highest promises in this regard, as these cathodes can deliver a specific energy approaching ~1000 Wh·kg<sup>-1</sup> at the material-level. These materials can potentially replace the currently used NMCs (e.g. LiNi<sub>0.6</sub>Mn<sub>0.2</sub>Co<sub>0.2</sub>O<sub>2</sub>, ~700 Wh·kg<sup>-1</sup>). Thanks to a decade of intense research, it is now well established that the anomalous extra capacity of Li-rich cathodes arises from the redox of O<sup>2-</sup> anions, more specifically the 'non-bonding' O 2p orbitals that point towards excess-Li in the metal layers.<sup>3–8</sup> Invigorated by this fundamental understanding, solid-state chemists have extended the concept of oxygen redox to cation-disordered  $Li_{1+\nu}M_{1-\nu}O_2$  (M = Nb, Mn, Ti, Fe, V ...) as well as Na-based layered oxides. 9-11 Despite this rich materials design-space, certain practical issues, such as voltage fade, poor kinetics, voltage hysteresis, and irreversible O2 loss, have delayed the commercialization of Li-rich NMCs.<sup>12</sup> Although the crucial role of oxygen redox towards these issues was clearly highlighted by detailed investigations on a 'practical' Li-rich NMC and also on a 'model' Li<sub>1,33</sub>Ru<sub>0.5</sub>Sn<sub>0.17</sub>O<sub>2</sub> electrode, much remains to be understood for further fundamental insights that will ultimately lead to implementable solutions. 12-14 Therefore, time has come to reinject the Li-rich systems with a fresh perspective towards the above-mentioned practical roadblocks observed in oxides. So far, only two materials-composition parameters were explored in Li-rich layered oxides, i.e. (i) going down from 3d Mn to 4d Ru and 5d Ir for stabilizing oxygen redox and (ii) increasing the Li-rich character to access higher capacity (e.g. Li<sub>3</sub>IrO<sub>4</sub>). <sup>15-17</sup> More recently, a third approach with mild success has emerged, that is to tune the ligand by increasing electronegativity of the anionic sublattice via substituting fluorine for oxygen, but so far limited only to disordered rocksalt structures. 18,19 Herein, we decided to explore a fourth direction by replacing the ligand oxygen with sulfur to design new Li-rich layered sulfides. Because sulfur is larger, softer and less electronegative compared to oxygen, anionic redox in sulfides can be expected to behave differently and possibly provide clues towards better performances.

Early sulfide electrodes, although long forgotten after the emergence of layered oxide cathodes, played a crucial historical role. To recall, the path towards modern Li-ion technology was paved by attempts of commercialization of Li-free layered transition-metal chalcogenides, such as TiS<sub>2</sub>, MoS<sub>2</sub> etc., way back in the 1970s, which was rapidly terminated because of safety issues due to Li-metal dendrite formation.<sup>20,21</sup> Interestingly, unlike oxides, stable ligand-hole chemistry was well-known in sulfides, e.g., TiS<sub>3</sub> (believed to exist as Ti<sup>4+</sup>S<sup>2-</sup>(S<sub>2</sub>)<sup>2-</sup>), Fe<sup>2+</sup>(S<sub>2</sub>)<sup>2-</sup>, etc., since the pioneering works by Rouxel *et al.*<sup>22,23</sup> In such materials, S exists fully or partially as dimerized S<sup>-</sup>—S<sup>-</sup> pairs and undergoes breaking of S—S bonds to regain the standard S<sup>2-</sup> state upon electrochemical insertion of Li.<sup>24-29</sup> However, Li (de)intercalation is only partly reversible in such materials besides rapid capacity fading.<sup>30-32</sup> Further studying the poly-sulfides such as TiS<sub>4</sub> and VS<sub>4</sub>, mainly for their conversion-type mechanism leading to large capacities at low potential, researchers have noted that such compounds were also enlisting sulfur redox activity.<sup>33-37</sup> Similarly, by reinvestigating the crystalline LiMS<sub>2</sub> (M = Ti, V, Cr, Fe) layered sulfides directly prepared from solid-state reactions, scientists also found that in some of these phases, both Li removal and insertion are possible, but it remains unclear whether the process involves anionic besides cationic redox activity.<sup>38-40</sup> Thus,

deciphering the sulfur redox process in such compounds could be of paramount importance to further understand the oxygen redox in Li-rich layered oxides.

80

81

82

83

84

85

86

87

88

89

90

91 92

93

94

95

96

97

98

99

100

101

102

103

104105

106

Li-rich NMCs are derived from the layered Li<sub>1,33</sub>Mn<sub>0.67</sub>O<sub>2</sub> (commonly written as Li<sub>2</sub>MnO<sub>3</sub>) with their anionic redox activity being a function of the competition between U(d-d coulomb interaction) and  $\Delta$ (charge transfer) terms.<sup>41</sup> Preparing a similar Li-rich Mn-based layered sulfide is not possible, simply because the S 3p band is situated much closer to the Li/Li<sup>+</sup> reference than the O 2p band, leaving the Mn<sup>3+/4+</sup> redox band too low-lying, see Figure 1a,b. Hence to design an analogous layered sulfide Li<sub>1.33</sub>M<sub>0.67</sub>S<sub>2</sub>, an appropriate transition metal M needs to be chosen first. Amongst 3d metals,  $M = Ti^{4+}$  presents the best choice for sulfides, because the  $Ti^{3+/4+}$  redox band is located above the S 3p band. However, since  $Ti^{4+}$  has  $3d^0$  electronic configuration, Li<sub>1.33</sub>Ti<sub>0.66</sub>S<sub>2</sub> is apparently electrochemically inactive, as shown recently, even though it has a high theoretical capacity of 339 mAh·g<sup>-1</sup> (considering removal of all Li's).<sup>42</sup> This situation reminds that of the Li<sub>1.33</sub>Mn<sub>0.67</sub>O<sub>2</sub> phase (poor electrochemical performance without nano-sizing) that required partial substitution with Ni<sup>2+</sup> to instigate electrochemical activity (Figure 1a).<sup>43–45</sup> A first hint to address this problem in sulfides consists, as discussed by Li et al., in using Co<sup>2+</sup> as a substituent (owing to its large U and small  $\Delta$ ) to initiate reversible anionic redox. Pursuing their idea, the authors succeeded in preparing Li<sub>1.2</sub>Ti<sub>0.6</sub>Co<sub>0.2</sub>S<sub>2</sub> showing anionic redox activity. 42 Other successful strategies to adjust proper band positioning have consisted in either preparing Ti<sup>3+</sup>-doped Li<sub>1.33-\(\nu\)/3</sub>Ti<sup>4+</sup><sub>0.67-\(\nu\)/3</sub>Ti<sup>3+</sup>\(\nu\)S<sub>2</sub>, or triggering antisite occupation as shown for NaCr<sup>3+</sup>S<sub>2</sub>, or preparing Li<sub>1,33</sub>Ti<sup>4+</sup><sub>0,67</sub>S<sub>2</sub> and Li<sub>1,5</sub>Nb<sup>5+</sup><sub>0,5</sub>S<sub>2</sub> having disordered rocksalt structures. 46-49 We herein demonstrate the feasibility to activate the anionic redox activity in Li-rich layered  $\text{Li}_{1,33-2\nu/3}\text{Ti}^{4+}_{0,67-\nu/3}\text{Fe}^{2+}_{\nu}\text{S}_2$  via the use of Fe substitution. This situation is favourable for reversible sulfur redox, since the Fe<sup>2+/3+</sup> redox couple with available electrons (3 $d^6$ ) is expected to be pinned at the top of the S 3p band (Figure 1c). 38 We isolate the Li<sub>1.13</sub>Ti<sub>0.57</sub>Fe<sub>0.3</sub>S<sub>2</sub> compound showing, based on cumulated cationic and anionic redox activity, a sustained reversible capacity of ~245 mAh·g<sup>-1</sup> at an average voltage of ~2.5 V, hence leading to a specific energy of ~600 Wh·kg<sup>-1</sup> that compares favorably with LiCoO<sub>2</sub>. Moreover, we demonstrate the advantages of choosing a softer ligand in partially mitigating both voltage fade and hysteresis without any compromise in kinetics, hence providing confidence about the feasibility of better capitalizing on the benefits of the anionic redox.

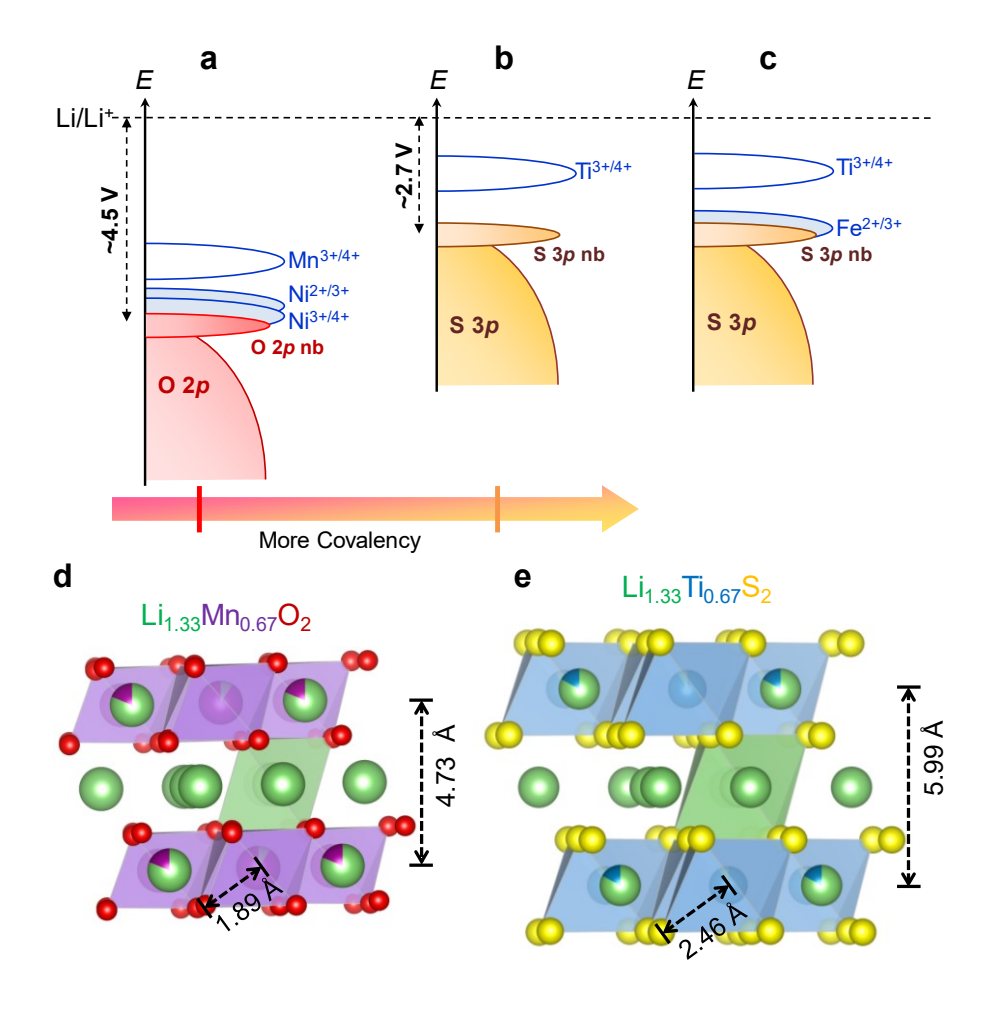


**Figure 1. Moving from Li-rich layered oxides to sulfides.** Schematic band structure of Ni<sup>2+</sup> substituted Li<sub>1.33</sub>Mn<sub>0.67</sub>O<sub>2</sub> (a) and Li<sub>1.33</sub>Ti<sub>0.67</sub>S<sub>2</sub> (b) and its Fe<sup>2+</sup> substituted derivative (c). The relative band positions are estimated based on *Ref* <sup>3,38</sup>. The label *nb* stands for non-bonding. The crystal structures of Li<sub>1.33</sub>Mn<sub>0.67</sub>O<sub>2</sub> (d, adapted from the *Ref* <sup>50</sup>) and Li<sub>1.33</sub>Ti<sub>0.67</sub>S<sub>2</sub> (e, this work), indicating the layer gap and the average metal-ligand bond distance.

### Results

Nominal compositions of Li<sub>1.33-2y/3</sub>Ti<sub>0.67-y/3</sub>Fe<sub>y</sub>S<sub>2</sub>, with y = 0 - 0.5, were prepared by reacting Li<sub>2</sub>S, TiS<sub>2</sub> and FeS in stoichiometric amounts in vacuum-sealed quartz tubes at 750 °C (see the Experimental Section for details). The X-ray diffraction (XRD) patterns are gathered in Figure S1a for all the compositions. The XRD pattern of the unsubstituted Li<sub>1.33</sub>Ti<sub>0.67</sub>S<sub>2</sub> (without Fe, y = 0) phase could be refined in the in C2/m space group alike for Li<sub>1.33</sub>Mn<sub>0.67</sub>O<sub>2</sub>. The Rietveld refinement of its synchrotron XRD (SXRD) pattern is shown in Figure S1b with the obtained parameters summarized in Table S1. This crystal structure is similar to honeycomb-ordered Li-rich layered oxides, however with an expectedly larger unit cell to accommodate the bulkier S atoms, see Figure 1d,e. Upon increasing the Fe content y, there is a progressive shift of the Bragg peaks (Figure 2a) indicating the existence of a solid solution. Moreover, Fe-containing compositions (y = 0.1 - 0.5) do not show the superstructure peaks (Figure S1a), most likely because Fe<sup>2+</sup> disrupts the honeycomb Li<sup>+</sup>/Ti<sup>4+</sup> ordering. Therefore, the Fe-containing phases could be fitted in a hexagonal

 $R\overline{3}m$  description analogous to the well-known Li-rich layered Li<sub>1+y</sub>M<sub>1-y</sub>O<sub>2</sub> phases, with the obtained lattice parameters shown in Figure 2b. With increasing Fe content, we observe a monotonic increase in the c parameter that is accompanied by a decrease in the a parameter, such that the overall effect is a monotonic decrease in unit cell volume (V). Since among the Li<sub>1.33-2y/3</sub>Ti<sub>0.67-y/3</sub>Fe<sub>y</sub>S<sub>2</sub> series, the compound with y = 0.3 will be the center of interest in this study, we also performed the Rietveld refinement of its SXRD pattern (Figure 2c), which confirms that Fe, Ti and Li occupy same site in the metal layer (see the structural model in Table S2). This structure was further confirmed by Rietveld refinement of its neutron powder diffraction (NPD) pattern (see Figure S5a).

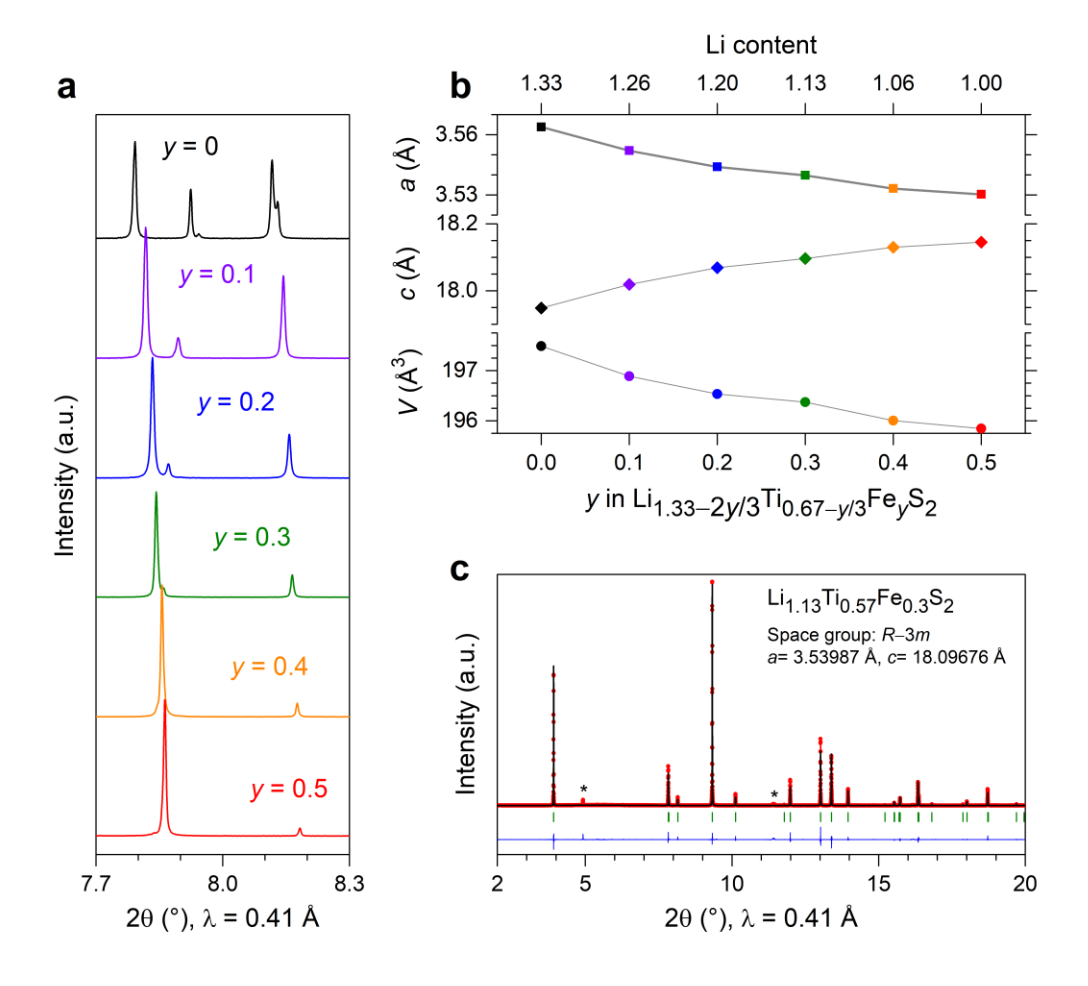


Figure 2. Structural behavior of the  $\text{Li}_{1.33-2y/3}\text{Ti}_{0.67-y/3}\text{Fe}_y\text{S}_z$  series. (a) SXRD patterns and (b) variation of lattice parameters (obtained from the Rietveld refinement of the SXRD patterns). In (b), for the y=0 composition, the lattice parameters have been converted to the  $R\overline{3}m$  description. (c) Rietveld refinement of the SXRD pattern of the  $\text{Li}_{1.13}\text{Ti}_{0.57}\text{Fe}_{0.3}\text{S}_2$  sample. The red circles, black continuous line, blue line, and green tick bars represent the observed, calculated and difference patterns, and Bragg positions, respectively. Note that minor  $\text{Li}_2\text{TiO}_3$  impurity (indicated with \*) was detected in the SXRD pattern, probably due to minor air-leakage during the preparation of the sample-capillary prior to the acquisition of SXRD patterns.

The electrochemical performances of the  $Li_{1.33-2\nu/3}Ti_{0.67-\nu/3}Fe_{\nu}S_2$  samples were tested in Li-half cells between 1.8 V and 3 V at a rate of C/20 and the voltage profiles are summarized in Figure 3a and S2a. The unsubstituted Li<sub>1.33</sub>Ti<sub>0.67</sub>S<sub>2</sub> ( $\nu = 0$ ) shows very poor electrochemical activity since only 0.1 Li could be extracted reversibly. Attempts to enhance the activity by either ball milling the samples or by adding larger amounts of carbon additive were unsuccessful, hence leading us to conclude that such a non-activity is intrinsic to the phase and most likely nested in the fact that the Ti<sup>3+/4+</sup> redox band is empty and is situated far above the S 3p band, hence unable to stabilize oxidized sulfur (Figure 1b). This contrasts with the Fe<sup>2+</sup>containing phases (Figure 1c) that are electrochemically active, which show a specificity that is nested in the second cycle's charge trace which mismatches the first one because it occurs at a lower potential (Figure 3a). Note also the appearance of a short sloped voltage (marked by 'S' in Figure 3a) at the early stage of charge, and most likely related to Fe redox activity. This contrasts with a long plateau-like (marked by 'P') activity on further oxidation. Lastly, the corresponding dO/dV profiles are shown in Figure 3b and S2c, which clearly highlights that the respective oxidation potentials shift to lower voltage with a systematic decrease in hysteresis (Figure S2e) upon increasing the Fe content. After the first cycle, note that the subsequent charge and discharge profiles are very similar (see Figure S2b for Li<sub>1.13</sub>Ti<sub>0.57</sub>Fe<sub>0.3</sub>S<sub>2</sub>) with the polarization gradually reducing to  $\sim 100$  mV for the y = 0.3 composition, instead of  $\sim 220$  mV during the first cycle. This indicates that the first cycle acts as an 'activation' cycle alike the Li-rich NMC oxides. The variation of capacity as a function of the Fe-content shows a bell-shape type behaviour which peaks at 245 mAh·g<sup>-1</sup> for the composition Li<sub>1,13</sub>Ti<sub>0.57</sub>Fe<sub>0.3</sub>S<sub>2</sub> (y = 0.3). Even by assuming full utilization of the multielectron oxidation of Fe<sup>2+</sup> to Fe<sup>4+</sup>, which is quite unlikely to occur in sulfide frameworks, we cannot account for all the measured capacity, hence implying the activity of the anionic network, see Figure 3c. The capacity decrease beyond y > 0.3 is simply due to the lower amount of available Li in the Li<sub>1,33-2v/3</sub>Ti<sub>0,67-v/3</sub>Fe<sub>v</sub>S<sub>2</sub> samples when the Fe content (y) increases. In contrast the raise noted until y = 0.3 is most likely nested in the gradual amelioration of the band positioning with introduction of Fe content that triggers reversible anionic redox activity. Among the various Fe compositions studied, the y = 0.3 sample not only shows the largest capacity, but also a respectable capacity retention (Figure 3d and S2d) with also barely noticeable irreversible capacity in the first discharge. Thus, we chose this composition for further investigation, starting by exploring whether the activation process over the first cycle is related to structural aspects.

141

142143

144

145

146147

148

149150

151

152

153154

155

156

157

158

159

160 161

162163

164

165

166167

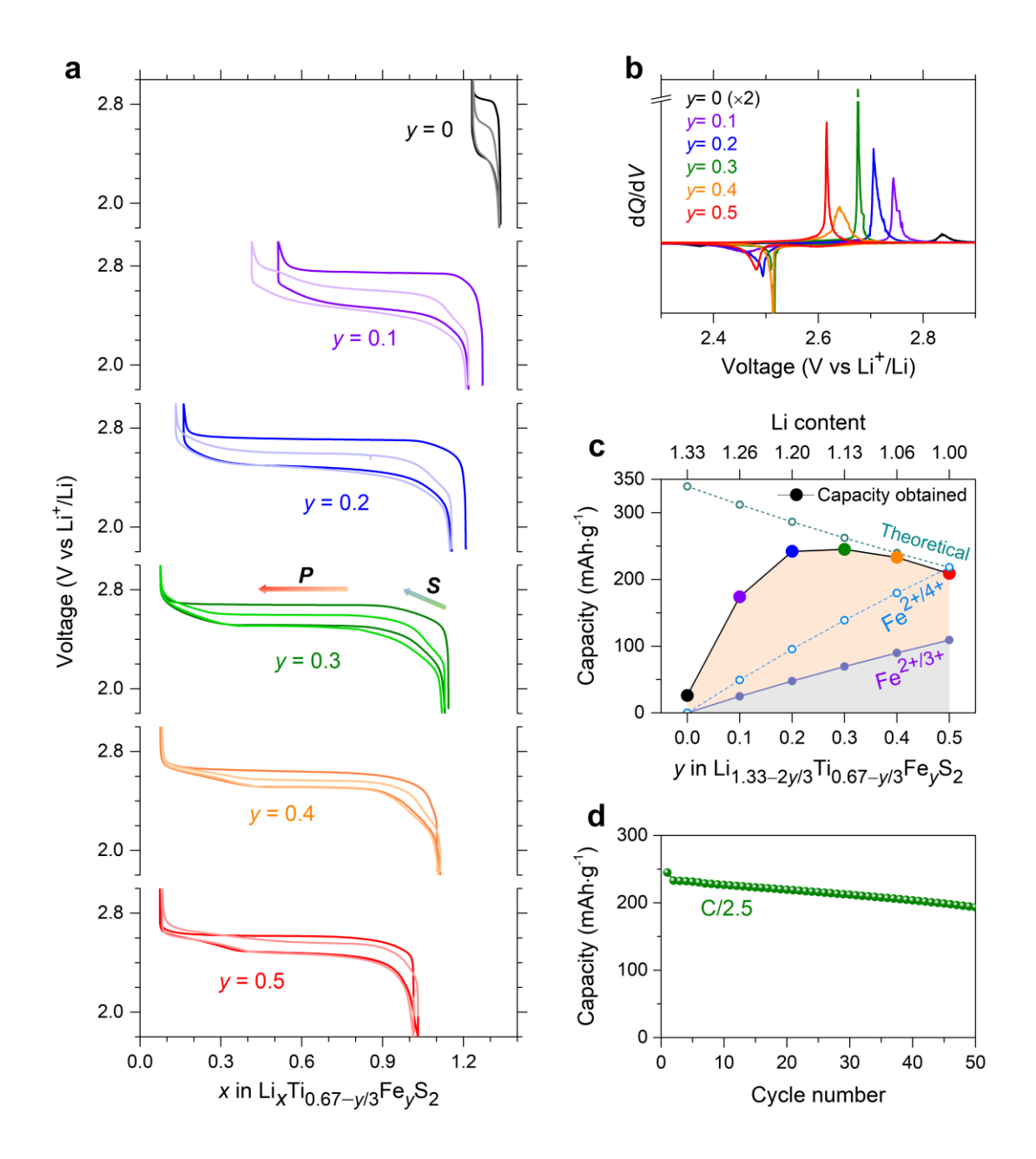


**Figure 3. Electrochemical behavior of Li**<sub>1.33-2y/3</sub>**Ti**<sub>0.67-y/3</sub>**Fe**<sub>y</sub>**S**<sub>2</sub>. (a) Voltage profiles of the compositions obtained over cycling vs Li at C/20 for the first two cycles. The curves in lighter colors denote the second cycles. The arrows marked by 'S' and 'P' denote the slope and the plateau, respectively. (b) dQ/dV curves obtained in the first cycle for the various compositions. (c) Theoretical capacity (considering total Li-removal) and the actual discharge capacity obtained for the compounds over cycling at C/20. The capacity expected from cationic Fe<sup>2+/3+</sup> and hypothetical Fe<sup>2+/4+</sup> redox is also shown. (d) Cycling performance of a Li<sub>1.13</sub>Ti<sub>0.57</sub>Fe<sub>0.3</sub>S<sub>2</sub>/Li half-cell at a rate of C/2.5 (except the first formation cycle at C/20). The material was cycled as powder (mixed with 20 wt% C, see Figure S2d inset) in a Swagelok type cell, without any further optimization.

To better understand the structural evolution pertaining to the Li<sub>1.13</sub>Ti<sub>0.57</sub>Fe<sub>0.3</sub>S<sub>2</sub> phase during the Li uptake-removal process, operando XRD measurements were conducted and XRD patterns were collected for every change in lithium stoichiometry of  $\sim 0.1$  (Fig. 4). Upon charge, we observed a slight initial shift of the main peaks, indicating solid-solution behaviour. Over this regime, the unit cell volume decreases as a consequence of an anisotropic variation of the a and c lattice parameters (see also, Figure S3a). Then, as the voltage reaches the first plateau, there is a gradual change in the intensity of the peaks with some peaks disappearing at the expense of new ones, which sharpen to give a well-defined XRD powder pattern at the end of the full charge, hence suggesting a two-phase de-intercalation process. This new phase with approximate composition Li<sub>0.13</sub>Ti<sub>0.57</sub>Fe<sub>0.3</sub>S<sub>2</sub>, whose structure remains as layered one as described in detail in the next paragraph, has a lower unit cell volume (by ~12.2%) than the pristine one. On discharge, the compound undergoes first a solid-solution process for which both the a and c lattice parameters strongly increase (Figure S3a). Then, a biphasic process is observed with the growth of a phase with increased volume, followed again by solid-solution behaviour. We therefore have, for the first cycle, charge and discharge processes that proceed through different structural paths, even though the pattern returns close to the one for the pristine phase (see Figure S3b). This path-difference can be clearly observed from the evolution of the unit cell volume (Figure 4a) and of the a and c lattice parameters (see Figure S3a). On the other hand, over the 2<sup>nd</sup> cycle, the XRD patterns indicate more symmetric, although not perfect, pathways on charge and discharge (Figure S4). Overall, throughout cycling the phase remains crystalline with wellpreserved long-range layered crystal structure.

Next, an in-depth exploration of the crystal structures at different states of charge (pristine, fully-charged and fully-discharged after first cycle) was undertaken using SXRD. In agreement with the lab XRD data, the patterns can be indexed in the  $R\overline{3}m$  space group. The pristine Li<sub>1.13</sub>Ti<sub>0.57</sub>Fe<sub>0.3</sub>S<sub>2</sub> (V=196.384(2) Å<sup>3</sup>) presents an average Ti–S bond-length of 2.4792(3) Å, with average S–S distances of ~3.505 Å (see the structural model in Table S2). The Rietveld refinement of the SXRD pattern of the fully-charged Li<sub>0.13</sub>Ti<sub>0.57</sub>Fe<sub>0.3</sub>S<sub>2</sub> phase (Figure 4b) indicates a much smaller unit cell (V=172.338(6) Å<sup>3</sup>) (see Table S3 for the structural model). Moreover the average Ti–S bond length was found to shrink to 2.3635(1) Å, leading to decreased average S–S distances of ~3.344 Å.

In parallel, we collected the selected-area electron diffraction (SAED) of the fully-charged phase which could again be successfully indexed with an  $R\bar{3}m$  unit cell (Figure S5b). The corresponding high angle annular dark field scanning transmission electron microscopy (HAADF-STEM) image shows only the (Ti/Fe)S<sub>2</sub> layers. The HAADF intensity profile (inset, Figure 4c) clearly demonstrates no scattering density between the (Ti/Fe)S<sub>2</sub> layers and thus discards the possibility of transition-metal migration to the interlayer sites (Figure 4c). The Rietveld refinement of SXRD pattern (Figure S5c, Table S4) of the fully-discharged sample is very similar to the pristine phase (V=196.896(2) ų) with an average Ti–S bond length of 2.4825(3) Å and average S–S distance of 3.51(2) Å. Worth mentioning is that such S–S distances are quite larger than the (S–S)²- bond lengths reported early on for TiS₃ (2.04 Å) (Figure 4d) suggesting either an absence of complete dimerization in Li<sub>0.13</sub>Ti<sub>0.57</sub>Fe<sub>0.3</sub>S<sub>2</sub> or a possible error in the reported TiS₃ structure. Further investigations focusing specifically on the local structure of such sulfide compounds are hence planned.

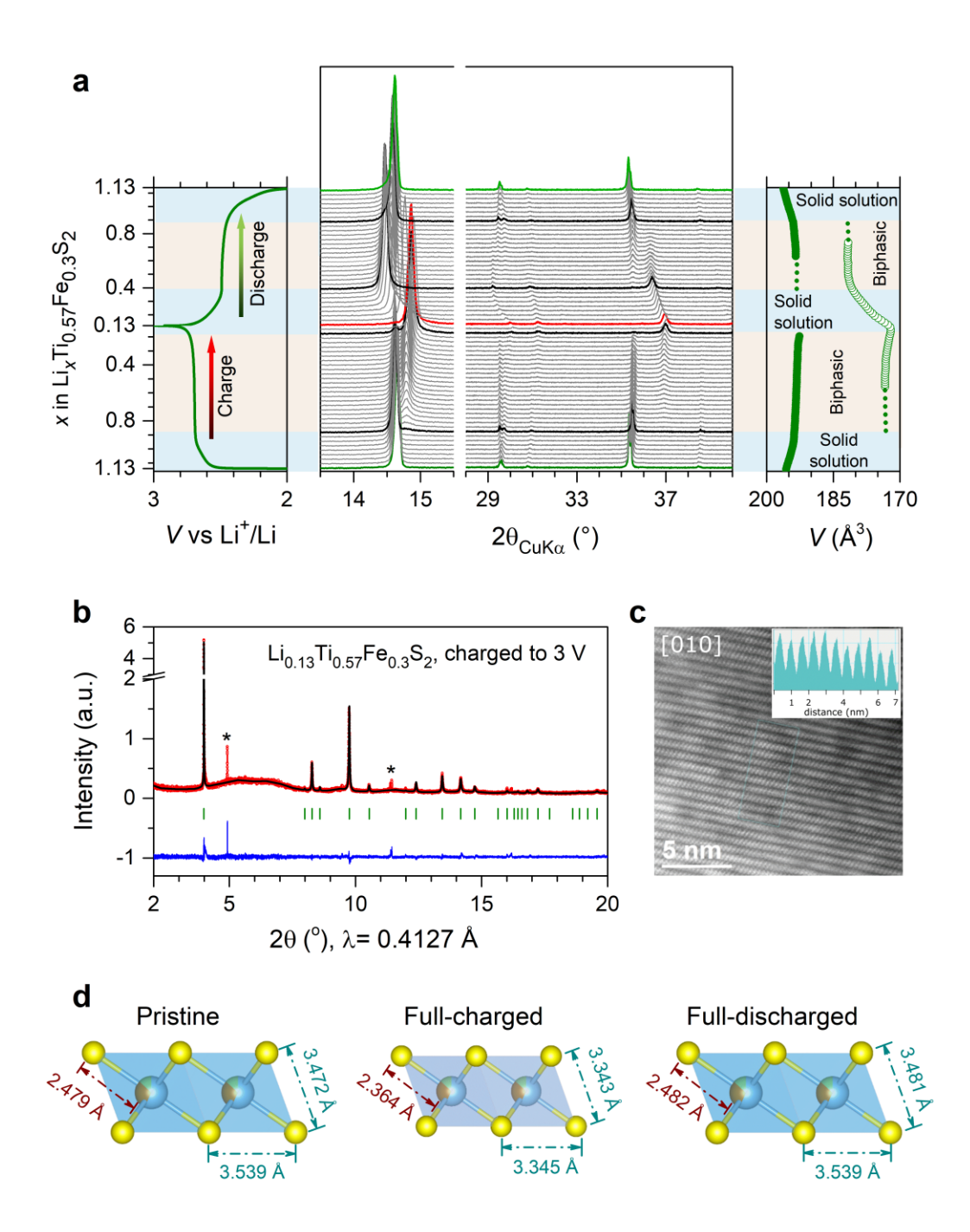


**Figure 4. Structural evolution upon Li (de)intercalation.** (a) Evolution of the *in situ* XRD patterns in the first cycle of a  $Li_{1.13}Ti_{0.57}Fe_{0.3}S_2$  /Li half-cell at a rate of C/20. The left panel shows the corresponding voltage profile and the right panel shows the evolution of the unit cell volume (V), as obtained from the Rietveld refinements of the XRD patterns. Note that the dotted lines represent extrapolations, where the XRD patterns could not be refined because of poor intensity of the peaks. (b-c) Rietveld refinement of the SXRD patterns (b) and the HAADF-STEM image (c) of the full-charged phase. The peaks denoted by \* in (b) show minor  $Li_2TiO_3$  impurity. The inset in (c) shows the HAADF intensity profile. (d) The bond-lengths observed in the pristine, full-charged and full-discharged phase (as obtained from the Rietveld refinement of the corresponding SXRD patterns).

To grasp some insights on the charge compensation mechanism, the cationic Fe<sup>2+/3+</sup> redox process was probed by operando Mössbauer spectroscopy using an electrochemical cell designed in-house.<sup>52</sup> Spectra were collected while charging and discharging a Li<sub>1.13</sub>Ti<sub>0.57</sub>Fe<sub>0.3</sub>S<sub>2</sub>/Li cell at a rate of C/70 (Figure 5). The Mössbauer spectra for pristine Li<sub>1.13</sub>Ti<sub>0.57</sub>Fe<sub>0.3</sub>S<sub>2</sub>, that can neatly be fitted with four doublets (see Table S5), highlights the presence of a distribution of high-spin (HS) Fe<sup>2+</sup>, as already encountered for FeS and various other iron (II)-based sulfides. 53,54 The necessity of four doublets is simply due to different local arrangements of intermixed Ti/Li/Fe cations around a given Fe site. The evolution of the spectra obtained during in situ cycling is shown as a contour plot in Figure 5b, with the spectra analyzed using principal component analysis (PCA), as described in Supplementary Note S1. All measured spectra could be adequately fitted as linear-combinations of three reconstructed spectral components. As expected, the first component (Comp. 1) is identical to the pristine material's spectrum. The Comp. 2 can be fitted using at least two doublets, see Figure 4a and Table S5. The major one (90%) has an isomer shift of 0.48 mm/s which stands between what is expected for HS Fe<sup>2+</sup> and HS Fe<sup>3+</sup>, alike what has been seen in Fe<sub>3</sub>S<sub>4</sub> and FeV<sub>2</sub>S<sub>4</sub>.<sup>53</sup> The second doublet with a 10 % contribution to the overall spectrum is indicative of the HS-Fe<sup>3+</sup> signature, as seen in NaFeS<sub>2</sub>.<sup>53</sup> Overall, the average oxidation state of *Comp. 2* is higher than Fe<sup>2+</sup> but not fully reaching Fe<sup>3+</sup>. Note that Comp. 2 reaches its maximum around  $x_{Li} = \sim 0.93$ , just before the voltage plateau. During the plateau, the Comp. 2 converts progressively to the Comp. 3 (fully-charged, 3 V), as shown in Figure 4c, in which can be fitted as low-spin Fe<sup>3+</sup> state in agreement with previous reports (Figure 4a and Table S5).<sup>40</sup> On discharge, the evolution of the components is reversed, except for a much lower contribution from the Comp. 2 (Figure 4a). This is fully consistent with the path dependence observed above with XRD. Overall, these data indicate the progressive oxidation of Fe<sup>2+</sup> to Fe<sup>3+</sup> on charge and its full reduction back to Fe<sup>2+</sup> on discharge.

225

226227

228

229

230

231

232

233234

235236

237

238

239

240

241

242

243

244245

246

247248

249

250

251

252

253

254

255

256

257

Furthermore, Fe  $L_{2,3}$ -edge X-ray absorption near edge structure (XANES) spectra were taken to confirm the participation of Fe and are shown in Figure S6b. The spectra for the pristine material is similar to that of FeS confirming the presence of Fe<sup>2+,55,56</sup> It enlists two main peaks corresponding to  $2p_{3/2} \rightarrow 3d$  ( $L_3$ ) and  $2p_{1/2} \rightarrow 3d$  ( $L_2$ ) transitions. These peaks shift to higher energy upon charge indicating gradual conversion to Fe<sup>3+</sup>. After discharge, the Fe  $L_{2,3}$  edge is restored completely. The position and shifts of the Fe  $L_{2,3}$ -edge observed upon oxidation are consistent with observations of S-containing species with Fe<sup>2+</sup> and Fe<sup>3+</sup> in literature, <sup>57</sup> indicating consistency with conclusions from Mössbauer spectroscopy. The Ti  $L_{2,3}$ -edge XANES spectra were also recorded for the aforementioned samples (Figure S6c). As expected, the spectrum for pristine Li<sub>1.13</sub>Ti<sub>0.57</sub>Fe<sub>0.3</sub>S<sub>2</sub> is identical to that of Ti<sup>4+</sup>S<sub>2</sub>, confirming the formal oxidation state of Ti as 4+. <sup>58</sup> Moreover, no changes in the position of  $L_2$  and  $L_3$  peaks could be observed, irrespective of the sample state of charge, hence indicating the invariance of Ti<sup>4+</sup> throughout the charge/discharge cycle. <sup>58</sup>

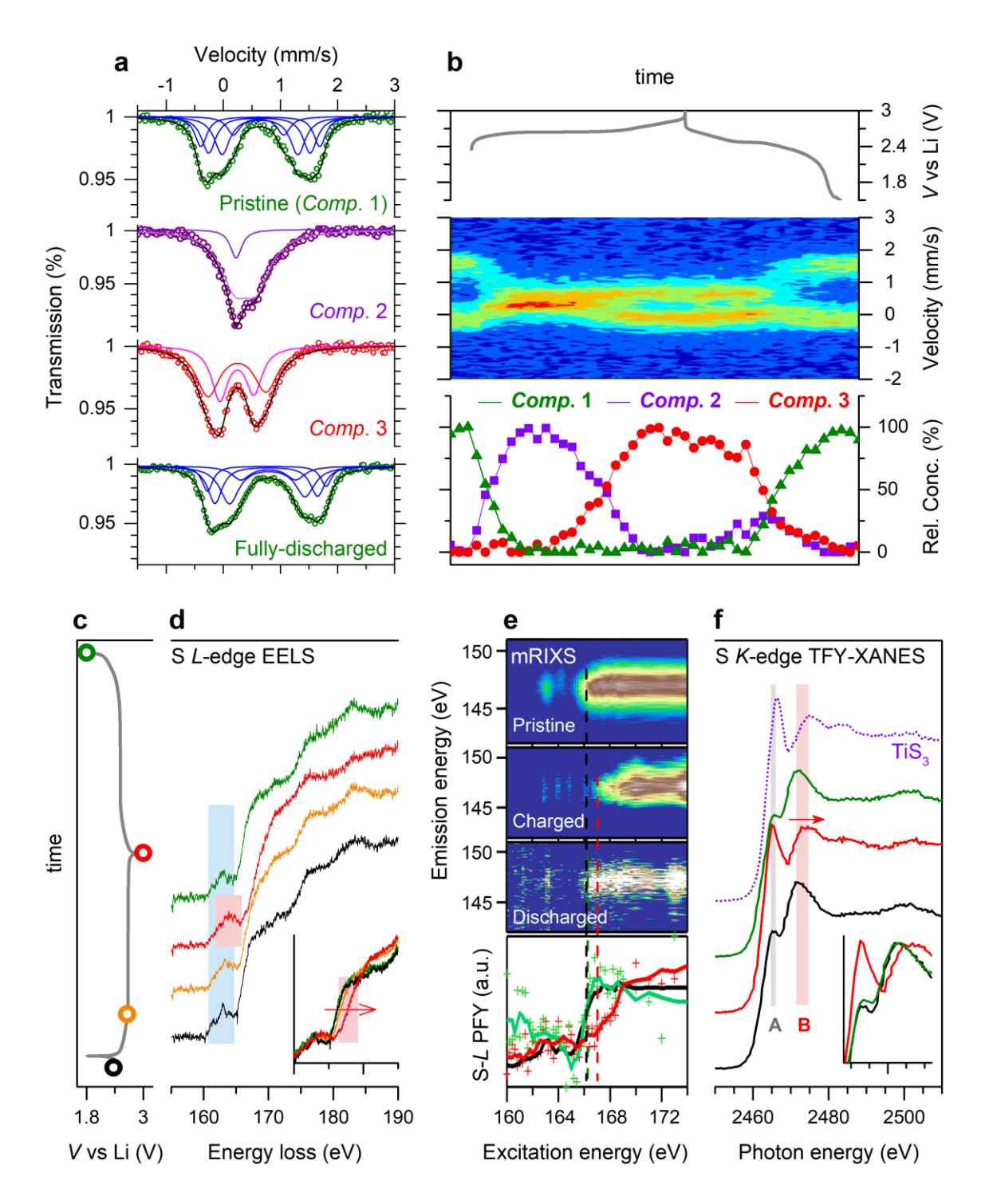


**Figure 5. Spectroscopic characterizations to identify the redox processes. (a)** Typical Mössbauer spectra and their deconvolution for the pristine (*comp*. 1), *comp*. 2, *comp*. 3 (fully charged) and the fully-discharged product. (b) Contour plot of evolution of the Mössbauer spectra collected during *in situ* cycling of a Li<sub>1.13</sub>Ti<sub>0.57</sub>Fe<sub>0.3</sub>S<sub>2</sub>/Li half-cell at a rate of C/70. For reference the voltage profile is shown in the top panel. The lowest panel shows the evolution of the reconstructed components during the cycling. (c-f) The EELS spectra of the S *L*-edge (d), mRIXS of the S *L*-edge with integrated PFY spectra on the bottom (e) and S *K*-edge XANES spectra (f) collected *ex situ* on the pristine (black curves), partially-charged (2.66 V, only EELS, orange curve), fully-charged (3 V, red curves) and fully-discharged phase (green curve) as shown in the voltage profile in (c).

To check the electrochemical activity of S within the Li<sub>1.13</sub>Ti<sub>0.57</sub>Fe<sub>0.3</sub>S<sub>2</sub> phase during the Li uptake and removal process, *ex situ* electron energy loss spectroscopy (EELS) spectra at the S  $L_{2,3}$  edge were collected (Figure 5d) for pristine, partially-charged (2.66 V, after removing ~0.16 Li), fully-charged (3 V) and fully-discharged (1.8 V) samples. The spectra consist of a weak pre-edge and an intense broad edge feature that correspond to a series of transitions from the S 2p core levels to unoccupied states.<sup>59</sup> The S  $L_{2,3}$  edge for the pristine material is similar to that of FeS indicating the predominance of S<sup>2-</sup> state (Figure 5d and S7a).<sup>59</sup> It remains nearly alike for the partially charged sample (at 2.66 V) with the exception of minor alterations that could be ascribed to a probable decrease of the Ti/Fe–S bond covalency. In contrast, for the fully-charged sample (at 3 V), the S  $L_{2,3}$  rising-edge shifts by ~1.6 eV towards higher energies and this is indicative of a partial oxidation of S<sup>2-,55</sup> However the S  $L_{2,3}$  pre-edge does not show the typical peak splitting seen in pyrite-FeS<sub>2</sub> or elemental S<sup>0</sup> (Figure S7b).<sup>56</sup> Lastly, it is worth mentioning that the initial shape as well as the energy of the rising-edge of the S  $L_{2,3}$  edge are fully recovered towards the end of the discharge, further indicative of the reversibility of the sulfur redox process.

While EELS data were collected locally on electrode microparticles processed vigorously in typical way (see method), we further probed the S L-edge by soft X-ray absorption spectroscopy (sXAS) to obtain more bulk-sensitive signature of sulfur redox. However, direct measurements of the electrodes on the S L-edge through conventional sXAS turned out to be challenging, because of large amount carbon present in the electrodes which contributes an overwhelming background through 2nd order harmonic around 140 eV, right below the S-L signals around 160 eV (Figure S7c,d). In order to distinguish the S signals from the strong C background, we employed high-efficiency mapping of resonant inelastic X-ray scattering (mRIXS, see Figure S7e), which further resolve the emitted photon energy, called emission energy, after each sXAS excitation process. 60 Figure 5e displays these S-L mRIXS signals collected from the pristine, fully-charged, and fully-discharged electrodes. The integration of all the signals within this emission energy range (142 -151 eV) provides the partial fluorescence yield (PFY) signals of the clean S-L sXAS. The results are summarized in the bottom panel, which is quite consistent with the EELS. The pristine Li<sub>1.13</sub>Ti<sub>0.57</sub>Fe<sub>0.3</sub>S<sub>2</sub> without carbon additive displays the strongest S-L features. The pre-edge peaks observed in EELS correspond to the relatively sharp features in mRIXS at 163 and 164.1 eV excitation energies. The sharp features suggest these are dominated by the localized TM 3d character that is hybridized with S orbitals.<sup>59</sup> Therefore, the continuous band-like feature at higher excitation energy correspond to the intrinsic sulfur states mixed with hybridization signals to TM 4s/4p orbitals. It is clear that the leading edge of these sulfur band-like feature shifts towards high energy for over 1.2 eV in the full charged phase, indicating the oxidation of sulfur states. The leading edge position completely recovers after discharge, as more clearly seen in the PFY summary, suggesting a reversible redox reaction of the sulfur.

S K-edge XANES spectra were equally collected for the aforementioned samples (except partially charged) and they are reported in Figure 5e. The spectrum presents two main regions. The pre-edge feature, below 2471 eV, arises generally from unoccupied S 3p/TM 3d hybridized states. Their position and intensity depend on their occupancy, the relative contribution of S and TM, and their position with respect to the core level, thus being a general measure of covalence of the TM-S bond. Above this energy, the signals correspond to transitions to higher states, such as S 3p/TM 4s, p or those involving S 4p, and the photoionization of S atoms, involving complete ejection of the core electron to the continuum. Therefore, the position of the absorption threshold is strongly dependent on the effective nuclear charge ( $Z_{eff}$ ) on S, being a measure of redox transitions at the ligands. The spectra for pristine Li<sub>1.13</sub>Ti<sub>0.57</sub>Fe<sub>0.3</sub>S<sub>2</sub> consists in a

weak pre-edge at ~2465 eV (denoted as **A**) and a broad edge jump (denoted as **B**) located at ~2472 eV similar to what is observed in amorphous rocksalt Li<sub>2</sub>TiS<sub>3</sub> and hence characteristic of S<sup>2-.48</sup> For the fully charged state (~Li<sub>0.1</sub>Ti<sub>0.57</sub>Fe<sub>0.3</sub>S<sub>2</sub>), the spectrum (red curve in Figure 5e) undergoes notable changes with an increase in amplitude of the pre-edge **A** and a ~1.2 eV shift of the **B** edge towards higher energy, and bears resemblance to TiS<sub>3</sub> (dashed purple curve).<sup>62</sup> Similarly, the opposite shift in the edge **B** is observed during re-lithiation, as was reported for TiS<sub>3</sub>, and VS<sub>4</sub>.<sup>36,63</sup> The 1.2 eV shift in **B** is therefore a clear indication of the oxidation of S<sup>2-</sup> into S<sup>n-</sup>, n < 2. Similarly, the increase in intensity of pre-edge **A** is indicative of the increase in density of unoccupied states just above the Fermi level with an S character, in agreement with the expectation that the redox change is compensated by S 3p/Fe 3d electrons. The shift of the main absorption edge also suggests that this compensation, and the resulting states, have a significant S character. This unambiguously confirms the participation of S in the overall electrochemical activity of Li<sub>1.13</sub>Ti<sub>0.57</sub>Fe<sub>0.3</sub>S<sub>2</sub> together with its reversibility since the S *K*-edge XANES spectra of the fully-discharged and pristine samples nearly superimpose (Figure S6d).

To confirm the above observations S 2p core X-ray photoelectron spectroscopy (XPS) spectra were also taken and are shown in Figure S6e. Clear variations of the spectra are observed upon charging-discharging the samples. The S  $2p_{3/2-1/2}$  XPS core spectrum can be fitted with a single doublet (160.7 - 161.9 eV) attributable to S<sup>2-</sup> for the pristine material, as in the TiS<sub>2</sub> reference.<sup>64</sup> As the sample gets oxidized, the spectrum markedly changes, with namely the appearance of one extra doublet at higher binding energies (161.8 - 163.0 eV), which is indicative of the presence of oxidized S<sup>n-</sup> (n < 2), in light of early previous studies on TiS<sub>3</sub> that is well-known to contain partially oxidized sulfur.<sup>32,64</sup> On discharge, the XPS spectrum is almost restored to the pristine-like state, confirming the reversibility of the anionic redox process.

At this stage, mindful of the strong involvement of anionic redox in the charge compensation mechanism of Li<sub>1.13</sub>Ti<sub>0.57</sub>Fe<sub>0.3</sub>S<sub>2</sub>, the next legitimate question pertains to the practicability of anionic redox in sulfides. Using these newly designed Li-rich sulfides as model compounds, we investigated whether some of the practical issues (large voltage hysteresis, sluggish kinetics and gradual voltage fade) that have so far plagued the commercialization of analogous Li-rich layered oxides showing anionic redox activity<sup>12,6</sup>, still persist when oxygen is replaced by sulfur. To assess the practical figures of merit in Li-rich sulfides, we first performed a galvanostatic intermittent titration technique (GITT) experiment (Figure 6a) after initial seven cycles to stabilize the voltage profile. Li<sub>1,13</sub>Ti<sub>0,57</sub>Fe<sub>0,3</sub>S<sub>2</sub> shows the disappearance of voltage hysteresis in the open-circuit voltage (OCV) throughout the cycle (only ~30 mV gap remains after just 30 mins of relaxation). This is a significantly better scenario than in Li-rich NMC (Li<sub>1.2</sub>Ni<sub>0.13</sub>Mn<sub>0.54</sub>Co<sub>0.13</sub>O<sub>2</sub>), where a severe OCV hysteresis up to 300 mV has been reported and further shown to be associated with oxygen redox (Figure 6b). 14 This performance is also better than the ~100 mV OCV hysteresis in 4d metal-based  $Li_2Ru_{0.75}Sn_{0.25}O_3$  and approaches the favorable hysteresis-free situation experienced in 5d metal-based  $\beta$ -Li<sub>2</sub>IrO<sub>3</sub>. <sup>13,16</sup> This observation clearly highlights that voltage hysteresis can be effectively mitigated by tuning the ligand, and not just by choosing appropriate transition metals. The hysteresis was further studied by progressive opening of voltage-windows during charge in subsequent cycles and the voltage profiles are summarized in Figure 6c. Increasing the voltage cut-off does not lead to any noticeable increase in voltage hysteresis. This contrasts with similar experiments on Li-rich NMC showing an onset of large hysteresis upon full charging accompanied with lowering of the discharge potential around mid-SoCs (Figure S8a). Furthermore, the corresponding dO/dV curves (in the inset, Figure 6c) reveal that irrespective of upper cutoff of charging voltage, in discharge the oxidative capacities are mostly recovered at ~2.5 V, therefore not triggering any voltage hysteresis. This is quite contrary to Li-rich NMC, where oxidative capacities obtained from anionic redox (i.e., charging above ~4.1 V) are only recovered partially at similar voltage upon discharge (down to  $\sim$ 4 V). Further discharge to a lower voltage (below  $\sim$ 3.6 V) is necessary to regain the remaining capacity, as the reduction of the oxidized  $O^{n-}$  species is split between high and low voltages, causing a large voltage hysteresis (Figure S8b).<sup>14</sup>

354

355356

357

358

359

360

361

362

363

364 365

366

367

368

369

370 371

372

373374

375

376

377

378

379

380

381

Concerning the next issue of kinetics, we have previously shown how oxygen redox displays sluggish kinetics. 13,14 Hence, to check the same in sulfides, cell resistance was deduced from the voltage drop during the first 10 s of the relaxation steps of the GITT experiment (Figure 6b). As revealed for Li<sub>1.13</sub>Ti<sub>0.57</sub>Fe<sub>0.3</sub>S<sub>2</sub>, the electrochemical resistance remains quite low throughout the whole cycle (Figure 6d). Whereas for Li-rich NMC, the resistance is significantly larger at all SoCs and increases at low and high SoCs, which corresponds to the regions involving oxygen redox. <sup>14</sup> Furthermore, electrochemical impedance spectra (EIS) were collected at different SoCs of Li<sub>1.13</sub>Ti<sub>0.57</sub>Fe<sub>0.3</sub>S<sub>2</sub>, after each relaxation step during the GITT experiment and the evolution of the EIS Nyquist plots is shown in Figure S9a,b. The charge-transfer resistance, located in the mid-frequency regime of the spectra (characteristic frequency around 10 to 1 Hz), remains very small and nearly constant throughout the cycle, irrespective of whether it is cationic or anionic redox regime, as opposed to Li-rich oxides where the resistance builds up drastically with deeper oxidation of oxygen. 12,14 This clearly highlights the positive attribute of Li-rich sulfides concerning kinetics. The fast kinetics was further confirmed with  $Li_1Ti_{0.5}Fe_{0.5}S_2$  (y = 0.5) composition, which shows similar charge transfer resistance and consequently similar cycling and rate performance (Figure S9c,d). Lastly, regarding the critical issue of voltage fade, we found that it still afflicts Li-rich sulfides, though to a much lower extent, as shown in Figure 6e. The voltage fade for Li<sub>1.13</sub>Ti<sub>0.57</sub>Fe<sub>0.3</sub>S<sub>2</sub> can be divided in two regimes, starting first with a well-pronounced decrease from 2<sup>nd</sup> cycle to the 7<sup>th</sup> (a drop of ~35 mV) followed by a stabilization afterwards to reach an overall drop of ~40 mV after 60 cycles (the maximum we have cycled). This again positively contrasts with Li-rich NMC that shows a nearly continuous voltage fade upon cycling with an accumulated drop of ~150 mV after 60 cycles. Overall, moving from oxygen to sulfur as the ligand turns out to be a correct strategy to partially mitigate the practical bottlenecks of anionic redox. However, we need to keep in mind that this comes at the expense of the overall energy density (Figure 6f) because of lower potential and higher molecular weight of sulfur. A compromise could consist in combining the energy advantage of oxygen redox with the practicability of sulfur redox. This task is not trivial bearing in mind the experienced difficulty in preparing 3*d*-metal-based oxysulfides.

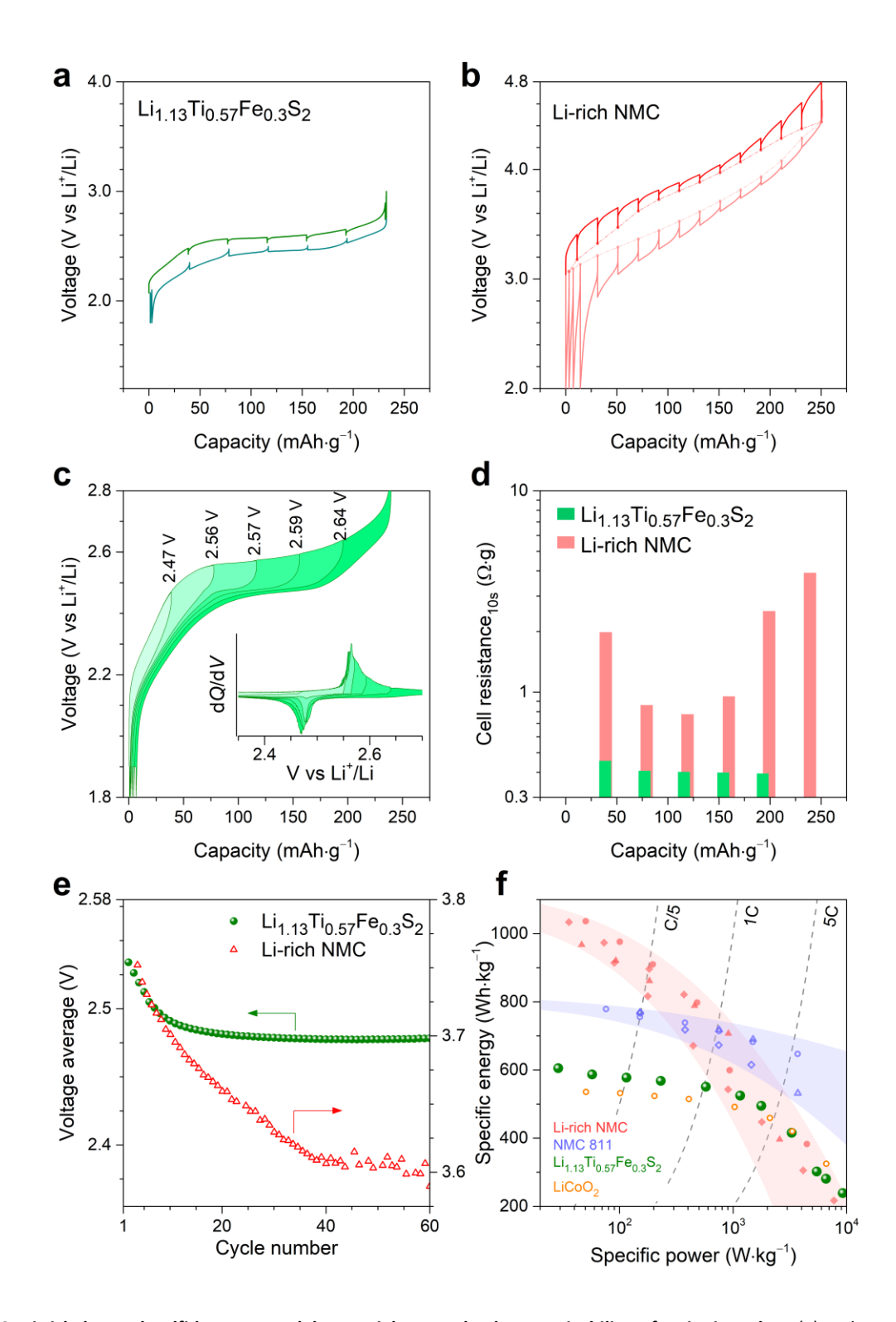


Figure 6. Li-rich layered sulfide as a model material to study the practicability of anionic redox. (a) Voltage profile of  $Li_{1.13}Ti_{0.57}Fe_{0.3}S_2$  in a two-electrode cell in the  $8^{th}$  cycle, recorded with a GITT protocol (C/5 rate with 30 min rests for equilibration). (b) Voltage profile of Li-rich NMC ( $Li_{1.2}Ni_{0.13}Mn_{0.54}Co_{0.13}O_2$ ) in a three-electrode cell in the  $4^{th}$  cycle, recorded with a GITT protocol (40 mA·g<sup>-1</sup> pulses with 4 h rests for equilibration). (c) Voltage profiles obtained from the charge-window opening experiment (starting from  $8^{th}$  cycle). Inset shows the corresponding dQ/dV profiles. (d) Cell's electrochemical resistance (during charging) estimated simply by Ohm's law from the voltage drop in first 10 s of rest from the previous GITT experiment in (a). (e) Average voltage during long cycling of  $Li_{1.13}Ti_{0.57}Fe_{0.3}S_2$  and Li-rich NMC in Li-half cells. In each cycle, the average voltage is defined as the

mean of the average charge and discharge voltages that and was calculated by dividing the energy with the capacity obtained. (f) Ragone plots of  $Li_{1.13}Ti_{0.57}Fe_{0.3}S_2$  and comparison with Li-rich NMC and Li-stoichiometric NMC ( $LiNi_{0.8}Mn_{0.1}Co_{0.1}O_2$ ). Only values at material-level are considered and values for the NMC-811 and the Li-rich NMC are adapted from *Reference*<sup>12</sup>. LiCoO<sub>2</sub> is also included in the comparison and the Li-rich layered sulfide appears at par with it.

#### **Discussion**

We have shown the feasibility, by partially substituting Ti<sup>4+</sup>/Li<sup>+</sup> belonging in the metal layers of Li<sub>1.33</sub>Ti<sub>0.67</sub>S<sub>3</sub> (commonly written Li<sub>2</sub>TiS<sub>3</sub>) with Fe<sup>2+</sup>, to produce Li<sub>1.33-2\(\nu\)/3</sub>Ti<sub>0.67-\(\nu\)/3</sub>Fe<sub>\(\nu\)</sub>S<sub>2</sub> phases showing electrochemical activity due to cumulated cationic (Fe<sup>2+/3+</sup>) and anionic (S<sup>2-</sup> / S<sup>n-</sup>, n < 2) redox processes. Alike the Li-rich layered oxides having  $d^0$  metals (Li<sub>2</sub>TiO<sub>3</sub>, etc...), we found the feasibility to trigger Li electrochemical activity in Li-rich layered sulfides having  $d^0$  metals by the injection of metal substituents. This does not come as a total surprise as such metal substitution modifies the U over  $\Delta$  competition, so that it falls within the domain to trigger reversible anionic redox activity as established from theoretical calculations. 41 The anionic redox activity upon oxidation was spectroscopically confirmed in  $\text{Li}_{1.13}\text{Ti}_{0.57}\text{Fe}_{0.3}\text{S}_2$  via clear energy shifts in the S  $L_{2.3}$ -edge EELS and XANES spectra as well as the onset of a doublet signal in the S  $2p_{3/2-1/2}$  XPS core spectra. Structure-wise on the other hand, our XRD and EELS evidence did not suggest the local formation of very short S-S dimers (like in pyrites), but more investigations focusing on the local structure are needed to unequivocally rule this out. For comparing with oxides, let's recall that the XPS fingerprint of anionic redox activity in oxides was also the appearance of a new component at slightly higher binding energy (531.5 eV) in the O 1s XPS core spectra that we assigned to  $O^{n-}$  (n < 2). <sup>14–16</sup> Interestingly, the binding energy of this component was independent of the structure and composition as seen in various Li-rich oxides that show anionic redox activity, with or without evidences of O-O shortening. This observation indicates that although XPS features have been widely used as the spectroscopic signature of the anionic redox activity in various materials, caution has to be exercised when interpreting XPS spectra.

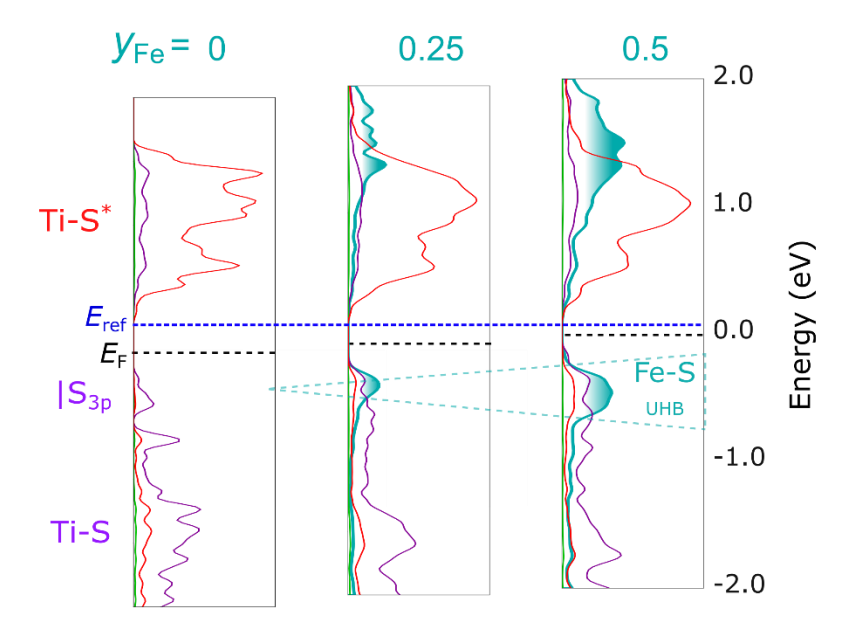
Besides, we found that Li<sub>1.13</sub>Ti<sub>0.57</sub>Fe<sub>0.3</sub>S<sub>2</sub> can deliver capacities as high as 245 mAh·g<sup>-1</sup> with a near-zero irreversible capacity during the first cycle as compared to ~0.2 Li for Li-rich 3*d* metal-based oxides (Figure S8c,d). This is consistent not only with the absence of cationic migration in sulfides, in contrast to some of the analogous oxides, but also with less severe changes observed between the first charge-discharge voltage profiles in Li<sub>1.13</sub>Ti<sub>0.57</sub>Fe<sub>0.3</sub>S<sub>2</sub> as opposed to Li-rich NMCs that show a staircase charging curve drastically changing to a S-shaped discharging curve. Lastly, part of the initial irreversibility in oxides is associated to a small amount of oxygen release from the surface, either directly as O<sub>2</sub> gas or indirectly by reacting with the electrolyte.<sup>3,65</sup> This is quite unlikely to occur with S which is a softer element as compared to O, therefore showing less reactivity and greater stability for the same degree of electrochemical oxidation.

We noted in the dQ/dV profile (recall Figure 3b) a systematic shift to lower potentials of the peaks corresponding to concomitant cationic and anionic redox processes with increasing Fe-content in Li<sub>1.33-2y/3</sub>Ti<sub>0.67-y/3</sub>Fe<sub>y</sub>S<sub>2</sub>, while for instance the position of the peaks was found to remain independent of Sn substitution in the Li<sub>2</sub>Ru<sub>1-y</sub>Sn<sub>y</sub>O<sub>3</sub> series showing well-decoupled cationic and anionic redox. <sup>15</sup> To understand this behaviour, we calculated the spin-projected density of states (pDOS) for y = 0, 0.25 and 0.5 (these compositions were chosen for ease of computation, see Methods) and plotted in Figure 7a. The electronic structure of the parent Li<sub>1.33</sub>Ti<sub>0.67</sub>S<sub>2</sub> displays a charge transfer gap between the empty Ti d band (in red), split by the crystal field, and the S band (in purple) formed of non-bonding S d states (denoted as d band (having six electrons), which is split by d-d Coulomb repulsion (introduced by a correction term d = 1.9 eV) into a deep-lying Lower Hubbard band (LHB), with five spin-up electrons, and an Upper Hubbard Band (UHB)

with one spin-down electron. This is consistent with the experimentally observed HS Fe<sup>2+</sup> from Mössbauer spectroscopy. The occupied states of the UHB lie above the  $|S_{3p}|$  states. As the Fe content increases, the number of these UHB states increases. If we take as a reference the energy ( $E_{ref}$ ) of states that are not expected to be directly affected by the Fe substitution, such as either the Ti-t<sub>2g</sub>\* that is close to the Fermi level (Figure 7a) or the S 3s core levels that are non-bonding and very deep in energy (see Figure S10a), we observe that the highest occupied states are rising in energy with Fe content as indicated by the raising of the Fermi level. This explains the experimental observation of voltage decrease with gradual Fe introduction.

Next we asked whether the experimentally observed electronic and structural changes upon Li removal could be supported by monitoring the evolution of pDOS and the corresponding theoretical S–S distances. This is answered by calculating the pDOS of Li<sub>x</sub>Ti<sub>0.58</sub>Fe<sub>0.25</sub>S<sub>2</sub> (1.17 >  $x_{Li}$ > 0.83) that is summarized in Figure 7b. At the beginning of charge (1.17 >  $x_{Li}$ > 0.83), the depletion of the Fe-UHB near the Fermi level indicates that Fe gets oxidized, while the average S–S distance remains unaffected and thus confirming that S acts as a spectator. This situation drastically changes upon further oxidation (0.83 >  $x_{Li}$ > 0.17) where the pDOS indicates the depletion of the S band near the Fermi level, which implies S undergoes partial oxidation. Over this composition range, the small decrease in some of the calculated S–S distances (marked in purple background in the histograms) and the progressive closing of the band gap suggests that the holes are delocalized over the S network through Fe-S interaction. The participation of S to the states right above the Fermi level significantly increased upon oxidation, consistent with the increase in pre-edge intensity observed by S *K*-edge XAS (Figure 5f).

## a) Increasing Fe content in $Li_{1.33-2y/3}Ti_{0.67-y/3}Fe_yS_2$



# b) Decreasing Li content in $Li_xTi_{0.58}Fe_{0.25}S_2$

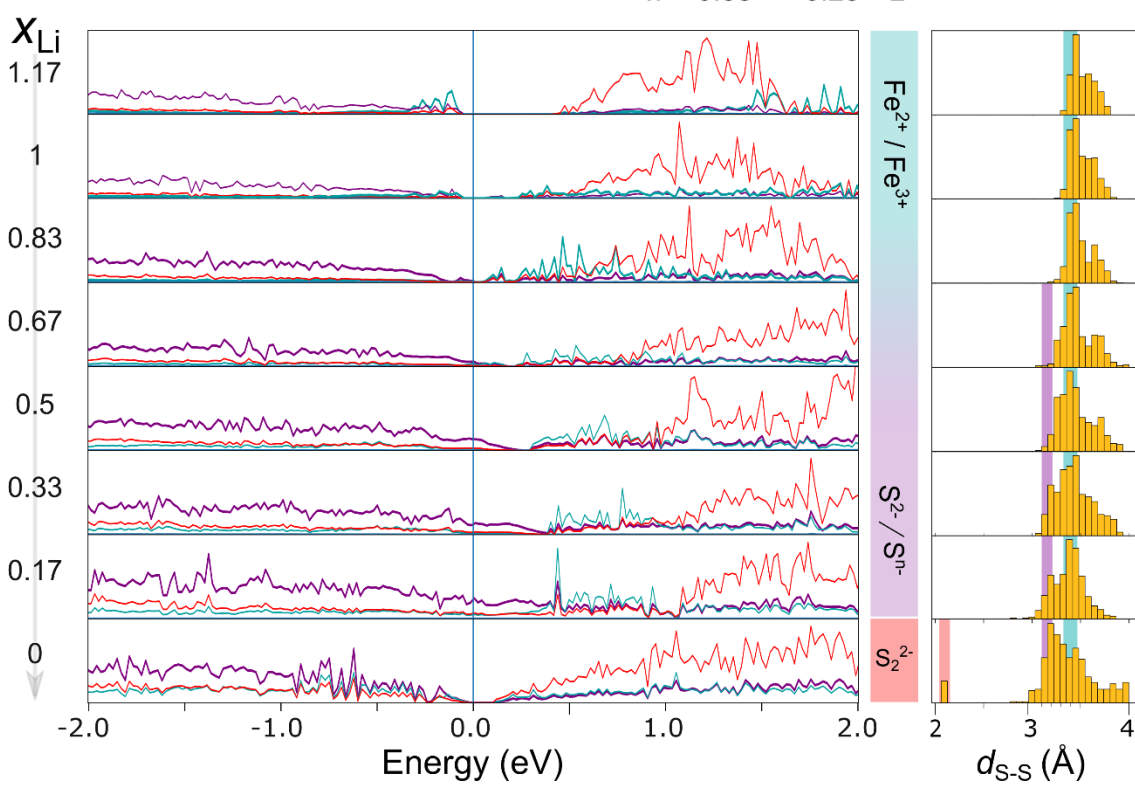


Figure 7. Correlating the experimental observations in  $\text{Li}_{1.33-2y/3}\text{Ti}_{0.67-y/3}\text{Fe}_y\text{S}_2$  with theoretical calculations. (a) Evolution of pDOS with increasing Fe content. Li, Ti, Fe and S contributions to bands are colored in light green, red, cyan and purple, respectively (b) Evolution of pDOS of  $\text{Li}_{1.17}\text{Ti}_{0.58}\text{Fe}_{0.25}\text{S}_2$  with Li-removal. The panel in middle indicates the deduced redox processes. The corresponding theoretically obtained S–S distances are shown in the histograms at right. The distances were chosen using a distance cut-off of 4 Å, without renormalization.

At high states of charge, the top of the highly dispersed sulfur band gets raised above the bottom of the empty Fe-UHB leading to electronic instability. This scenario triggers, if we simulate complete Li removal ( $x_{\text{Li}} \sim 0$ ), a reorganization of the network through the formation of true S–S dimers with a calculated bond length of ~2.1 Å (red background in the histogram). However, experimentally, full Li depletion is not observed since our fully oxidized sample still contains 0.13 Li<sup>+</sup> (~ Li<sub>0.13</sub>Ti<sub>0.57</sub>Fe<sub>0.3</sub>S<sub>2</sub>). In short, the participation of S in the redox process could unambiguously be confirmed theoretically, hence explaining the measured shortening of the S-S distances. However, the predicted dimerization at full charge could not be confirmed experimentally because the fully delithiated phase was not obtained electrochemically. This finding probably explains the excellent cycling reversibility of Li<sub>1.33-2y/3</sub>Ti<sub>0.67-y/3</sub>Fe<sub>y</sub>S<sub>2</sub>, as opposed to TiS<sub>3</sub>, where the cleavage of the S–S dimers leads to huge rearrangements of the crystal structure, resulting to rapid capacity fading with cycling.<sup>30-32</sup> Nevertheless, the question of (S<sub>2</sub>)<sup>2-</sup> vs. S<sup>n-</sup> (n < 2) upon complete delithiation remains to be fully elucidated, which will likely trigger more detailed characterizations and theoretical calculations on various sulfide materials in the future.

In summary, a new class of Li-rich layered sulfides Li<sub>1,33-2,y/3</sub>Ti<sub>0,67-y/3</sub>Fe<sub>v</sub>S<sub>2</sub> have been designed and studied for their electrochemical behaviour as cathode materials. Within this series, the phase Li<sub>1.13</sub>Ti<sub>0.57</sub>Fe<sub>0.3</sub>S<sub>2</sub> offers the largest reversible capacity (245 mAh·g<sup>-1</sup>) and we have shown, via complementary Mössbauer, XANES, EELS, mRIX and XPS spectroscopies, that this capacity mainly originates from sulfur redox besides the cationic redox of Fe. When benchmarking against Li-rich NMCs, this phase present several positive attributes such as (i) a nearly zero irreversible capacity during the initial cycle, (ii) an overall voltage fade as low as 40 mV even after 60 cycles and (iii) low voltage hysteresis (35 mV), along with fast kinetics, as compared to Li-rich NMC showing an irreversibility of ~0.2 Li, a voltage fade of 150 mV and a hysteresis of 300 mV besides sluggish kinetics. Energy-wise, these Li-rich layered sulfide positive electrodes display a specific energy of ~600 Wh·kg<sup>-1</sup> at the material-level while being composed of earth-abundant elements (3d metals only). This is much lower than the  $\sim 1000 \text{ Wh} \cdot \text{kg}^{-1}$ obtained for Li-rich NMC and thus they may not offer any real-world competitiveness against oxide electrodes furthermore due to their low operating potential as well as the practical issues with the handling of sulfides. Nevertheless, we believe that they could serve as excellent 'model' electrodes to study the general properties of anionic redox chemistry and in exploring kinetics, especially via the realization of Sbased solid-state batteries that can enable playing with temperature as an extra dimension. Both low hysteresis and structural integrity upon Li (de)intercalation are promising assets to design next-generation cathodes provided we can overcome the energy density penalty pertaining to the use of sulfur as a ligand. Preparing 3d-metal oxysulfides is an option if we ever overcome their synthesis difficulties. The door is wide-open for chemists to take forward this new dimension of exploring the effect of the ligand in enhancing the holistic performances of anionic redox in search for practical high-energy batteries.

#### **Experimental Section**

Synthesis. Li<sub>1.33-2y/3</sub>Ti<sub>0.67-y/3</sub>Fe<sub>y</sub>S<sub>2</sub> samples were prepared by solid-state reaction of stoichiometric amounts of Li<sub>2</sub>S (Alfa Aesar, 99.9%), TiS<sub>2</sub> (Sigma Aldrich, 99.9%) and FeS (Alfa Aesar, 99%). Homogeneously mixed and hand-grinded precursor powders were filled in quartz tubes in an Ar-filled glovebox followed by sealing the tubes under vacuum (~10<sup>-5</sup> mbar). The sealed tubes were subsequently annealed at 750 °C for 36 h followed by quenching in water. The as-prepared samples were collected inside a glovebox and hand-grinded prior to further use. In the whole process, air contact was avoided and subsequent processing was done in an Ar-filled glovebox. TiS<sub>3</sub>, used as a reference for XAS, was prepared similarly, by reacting TiS<sub>2</sub> and elemental S (15 wt% extra), in a vacuum sealed quartz tube at 550 °C, followed by cooling slowly.

**Structural Characterization.** Synchrotron X-ray powder diffraction (SXRD) patterns were collected at the 11-BM beamline of the Advanced Photon Source (APS), Argonne National Laboratory. All SXRD data were collected in transmission mode with  $\lambda = 0.4127$  Å, with the powder sealed in a quartz capillary of 0.7 mm diameter. Operando and *in situ* X-ray powder diffraction (XRD) was performed in an airtight electrochemical cell equipped with a Be window. XRD patterns were recorded in reflection mode in Bragg–Brentano geometry using a Bruker D8 Advance diffractometer equipped with a Cu-K $_{\alpha}$  X-ray source ( $\lambda_1 = 1.54056$  Å,  $\lambda_2 = 1.54439$  Å) and a LynxEye detector. The refinements of the patterns were done using the Rietveld method<sup>66</sup> as implemented in the FullProf program<sup>67</sup>.

Electrochemical characterization. Li<sub>1.33-2y/3</sub>Ti<sub>0.67-y/3</sub>Fe<sub>y</sub>S<sub>2</sub> samples were cycled in galvanostatic mode in Li half-cells assembled in Swagelok-type cells. The cathode materials were mixed with 20 wt% conductive carbon Super-P by hand-grinding for 5 min prior to cycling (Figure S2d inset). LP30 (1M LiPF<sub>6</sub> in ethylene carbonate/dimethyl carbonate in 1:1 weight ratio) was used as the electrolyte and was soaked in a Whatman GF/D borosilicate glass fiber membrane that was used as separator. Typical loadings of 10 mg of active materials were used and metallic Li was used as the negative electrode. The cells were assembled in an Ar-filled glovebox and were cycled at a C/20 rate between 1.8 V and 3 V if not specified otherwise. Charged/discharged samples from the Swagelok cells were recovered for *ex situ* characterizations by disassembling the cells inside glovebox, rinsed thoroughly with anhydrous DMC and dried under vacuum. All electrochemical cycling and EIS measurements (in 10 mHz – 200 kHz frequency range applying a 10 mV sinusoidal wave) were performed with BioLogic potentiostats.

Mössbauer spectroscopy. Room-temperature  $^{57}$ Fe Mössbauer spectra were recorded in transmission geometry in the constant acceleration mode and with a  $^{57}$ Co(Rh) source with a nominal activity of 370 MBq. The velocity scale ( $\pm 4 \text{ mms}^{-1}$ ) was calibrated at room temperature with α-Fe foil. The *in situ* cell was prepared with 32 mg.cm<sup>-2</sup> of active material mixed with 8 mg of carbon black. The hyperfine parameters IS (isomer shift) and QS (quadrupole splitting) were determined by fitting Lorentzian lines to the experimental data. The isomer shifts values are calculated with respect to that of α-Fe standard at room temperature. The obtained operando spectra were fitted using a statistical method based on Principal Component Analysis (PCA). This approach is a chemometric factor analysis tool able to determine the minimal particular structures in multivariate spectral data sets. Once the number of principal components is determined by PCA, a Multivariate Curve Resolution-Alternating Least Squares (MCR-ALS) algorithm is used for the stepwise reconstruction of the pure spectral components which are necessary for interpreting the whole multiset of operando Mössbauer spectra.

Energy loss spectra (EELS). The sample was prepared in an Ar-filled glove box by crushing the crystals in a mortar in DMC and depositing drops of the suspension onto holey carbon grids. The samples were transported to the transmission electron microscope (TEM) column while completely avoiding contact with air. High angle annular dark field scanning transmission electron microscopy (HAADF-STEM) images and EELS spectra were obtained with a FEI Titan G3 electron microscope operated at 120 kV and equipped with a monochromator and a Gatan Enfinium ER spectrometer. Energy resolution measured by full width at half maximum of the zero loss peak is 0.15 eV.

X-ray absorption spectroscopy (XAS). S K-edge, Fe L-edge and Ti L-edge X-ray absorption near edge spectroscopy (XANES) measurements were performed at 4-ID-C beamline of APS at Argonne National Laboratory. Spectra were recorded simultaneously under both the total electron yield (TEY) mode from the sample photocurrent at  $\sim 10^{-9}$  Torr and total fluorescence yield (TFY) mode using a silicon drift diode detector at a spectral resolution of  $\sim 0.2$  eV, with a 2 s dwell time. The energy scales of the spectra were calibrated with the references of Mo metal, Fe metal and SrTiO<sub>3</sub> measured simultaneously, for S, Fe and Ti edges, respectively.

**Soft X-ray absorption spectroscopy (sXAS) and mapping of resonant inelastic X-ray scattering (mRIXS).** The S *L*-edge sXAS and mRIXS experiments were performed in the iRIXS endstation of beamline 8.0.1 at the Advanced Light Source (ALS) of Lawrence Berkeley National Laboratory. <sup>69</sup> The pristine powder and cycled electrodes were mounted in high purity Ar glove box

and transferred into the experimental vacuum chamber through a home-made kit to avoid any air exposure. The experimental energy resolution of sXAS is better than 0.1 eV without considering the intrinsic core hole broadening (~0.2 eV). The energy resolution along the emission energy in mRIXS is about 0.2 eV,<sup>69</sup> which is sufficient for separating the intrinsic S-L signals from the strong C-K (2<sup>nd</sup> order) background that are different for about 10 eV. The X-ray exposure area on the samples were kept moving throughout the mRIXS experiments to avoid irradiation damage.

 X-ray photoemission spectroscopy (XPS). XPS spectra were collected on a sample (analyzed area =  $300 \times 700 \, \mu m^2$ ) with a Kratos Axis Ultra spectrometer, using focused monochromatic Al K $\alpha$  radiation ( $hv = 1.4866 \, keV$ ). The pressure in the analysis chamber was around  $5 \times 10^{-9}$  mbar. The binding energy scale was calibrated using the C 1s peak at 285.0 eV from the invariably present hydrocarbon contamination (for the pristine sample), and using the S<sup>2-</sup> position of the S  $2p_{3/2}$  at 160.7 eV for a better accuracy (for the other cycled samples). Peaks were recorded with constant pass energy of 20 eV. Core peaks were analyzed using a nonlinear Shirley-type background. The peak positions and areas were optimized by a weighted least-squares fitting method using 70 % Gaussian, 30 % Lorentzian line shapes. Quantification was performed on the basis of Scofield's relative sensitivity factors.

**Theoretical calculations.** Starting from a 221 supercell of Li<sub>2</sub>TiS<sub>3</sub> obtained from SXRD refinement, with honeycomb ordering of Li/Ti in the metallic layer, we achieved a composition of Li<sub>1.17</sub>Ti<sub>0.58</sub>Fe<sub>0.25</sub>S<sub>2</sub> (resp. Li<sub>1</sub>Ti<sub>0.5</sub>Fe<sub>0.5</sub>S<sub>2</sub>) by replacing 2 Li (resp. 4) and 1 Ti (resp. 2) atoms by Fe atoms. The atoms to replace were chosen to minimize the total Madelung energy of the final structure. To delithiate, we iteratively removed the Li atoms according to their Madelung energy (assuming integer oxidation state for every ion), using the Python Material Genome library. For each Li content, structures were then relaxed using the Vienna Ab-Initio Simulation Package using ultra-soft PAW pseudo potentials and the Perdew-Burke-Ernzerhof functional with a generalized gradient approximation. We added D3 correction to account for the van der Waals interaction so well as a  $U_{\text{eff}} = 1.9 \text{ eV}$  to account for electron–electron interactions on Fe. The forces on the atoms were converged to  $10^3 \text{ eV}\text{Å}^{-1}$  with a plane-wave energy cut-off of 600 eV and a well converged set of Kpoints.

**Acknowledgements:** S.S. thanks the Réseau sur le Stockage Electrochimique de l'Energie (RS2E) for funding of the Ph.D. J.-M.T. acknowledges funding from the European Research Council (ERC) (FP/2014)/ERC Grant-Project 670116-ARPEMA. Use of the 11-BM mail service of the APS at Argonne National Laboratory was supported by the US Department of Energy under contract No. DE-AC02-06CH11357 and is gratefully acknowledged. The authors thank M. Saubanère & M-L. Doublet for fruitful discussions and the laboratory Chimie Théorique Methodes & Modélisaion (CTMM) at the Institut Claude Gerhardt Montpellier (ICGM) for computational facilities.

#### 571 References:

- 572 1. Blomgren, G. E. The Development and Future of Lithium Ion Batteries. J. Electrochem. Soc. 164, A5019–A5025 (2017).
- 573 2. Schmuch, R., Wagner, R., Hörpel, G., Placke, T. & Winter, M. Performance and cost of materials for lithium-based rechargeable automotive batteries. *Nat. Energy* 3, 267–278 (2018).
- 575 3. Luo, K. *et al.* Charge-compensation in 3d-transition-metal-oxide intercalation cathodes through the generation of localized electron holes on oxygen. *Nat. Chem.* **8**, 684–691 (2016).
- 577 4. Koga, H. *et al.* Reversible Oxygen Participation to the Redox Processes Revealed for Li 1.20 Mn 0.54 Co 0.13 Ni 0.13 O 2. *J. Electrochem. Soc.* **160**, A786–A792 (2013).
- 5. Yabuuchi, N. Solid-state Redox Reaction of Oxide Ions for Rechargeable Batteries. Chem. Lett. 46, 412–422 (2017).
- 580 6. Seo, D.-H. *et al.* The structural and chemical origin of the oxygen redox activity in layered and cation-disordered Li-excess cathode materials. *Nat. Chem.* **8**, 692–697 (2016).
- 582 7. Saubanè, M., Mccalla, E., Tarascon, J.-M. & Doublet, M.-L. The intriguing question of anionic redox in high-energy density cathodes for Li-ion batteries. *Energy Environ. Sci.* 9, 984 (2016).
- 584 8. Okubo, M. & Yamada, A. Molecular Orbital Principles of Oxygen-Redox Battery Electrodes. *ACS Appl. Mater. Interfaces* **9**, 36463–36472 (2017).
- 586 9. Yabuuchi, N. *et al.* Origin of stabilization and destabilization in solid-state redox reaction of oxide ions for lithium-ion batteries. *Nat. Commun.* 7, 13814 (2016).
- 588 10. Maitra, U. *et al.* Oxygen redox chemistry without excess alkali-metal ions in Na 2/3 [Mg 0.28 Mn 0.72 ]O 2. *Nat. Chem.* **10**, 288–295 (2018).
- 590 11. Mortemard de Boisse, B. *et al.* Highly Reversible Oxygen-Redox Chemistry at 4.1 V in Na <sub>4/7-x</sub> [ $\square$  <sub>1/7</sub> Mn <sub>6/7</sub>]O <sub>2</sub> ( $\square$ : Mn Vacancy). 591 *Adv. Energy Mater.* **8**, 1800409 (2018).
- 592 12. Assat, G. & Tarascon, J. M. Fundamental understanding and practical challenges of anionic redox activity in Li-ion batteries. *Nat. Energy* **3**, 373–386 (2018).
- 594 13. Assat, G., Delacourt, C., Corte, D. A. D. & Tarascon, J.-M. Editors' Choice—Practical Assessment of Anionic Redox in Li-Rich Layered Oxide Cathodes: A Mixed Blessing for High Energy Li-Ion Batteries. *J. Electrochem. Soc.* 163, A2965–A2976 (2016).
- 596 14. Assat, G. *et al.* Fundamental interplay between anionic/cationic redox governing the kinetics and thermodynamics of lithium-rich cathodes. *Nat. Commun.* **8**, (2017).
- 598 15. Sathiya, M. et al. Reversible anionic redox chemistry in high-capacity layered-oxide electrodes. Nat. Mater. 12, 827–835 (2013).
- Pearce, P. E. et al. Evidence for anionic redox activity in a tridimensional-ordered Li-rich positive electrode β-Li2IrO3. Nat. Mater. 16, 580–586 (2017).
- Forez, A. J. *et al.* Approaching the limits of cationic and anionic electrochemical activity with the Li-rich layered rocksalt Li3IrO4. *Nat. Energy* **2**, 954–962 (2017).
- House, R. A. *et al.* Lithium manganese oxyfluoride as a new cathode material exhibiting oxygen redox. *Energy Environ. Sci.* **11**, 926 (2018).
- Lee, J. et al. Reversible Mn2+/Mn4+ double redox in lithium-excess cathode materials. *Nature* **556**, 185–190 (2018).
- Whittingham, M. S. Electrical Energy Storage and Intercalation Chemistry. *Science* (80-. ). 192, 1126–1127 (1976).
- Whittingham, M. S. Lithium batteries and cathode materials. Chem. Rev. 104, 4271–4301 (2004).
- Rouxel, J. Anion-cation redox competition and the formation of new compounds in highly covalent systems. *Chem. A Eur. J.* **2**, 1053–1059 (1996).
- 610 23. Rouxel, J. Some solid state chemistry with holes: Anion-cation redox competition in solids. Curr. Sci. 73, 31–39 (1997).
- Brec, R., Prouzet, E. & Ouvrard, G. Redox processes in the LixFeS2/Li electrochemical system studied through crystal, Mössbauer, and EXAFS analyses. *J. Power Sources* **26**, 325–332 (1989).
- Blandeaut, L., Ouvrardt, G., Calaget, Y., Brect, R. & Rouxelt, J. Transition-metal dichalcogenides from disintercalation processes.

- 614 Crystal structure determination and Mossbauer study of Li, FeS, and its disintercalates Li, FeS, (0.2 d x d 2). J. Phys. C: Solid State Phys **20**. (1987).
- 616 26. Onuk/, Y., Yamanaka, S. & Kamimura, H. ELECTROCHEMICAL CHARACTERISTICS OF TRANSITION-METAL TRICHAL COGENIDES IN THE SECONDARY LITHIUM BATTERY. Solid State Ionics 11, (1983).
- 618 27. Murphy, D. W. & Trijmbore, F. A. METAL CHALCOGENIDES AS REVERSIBLE ELECTRODES IN NONAQUEOUS LITHIUM BATTERIES. Journal of Crystal Growth 39, (1977).
- 620 28. Murphy, D. W. The Chemistry of TiS[sub 3] and NbSe[sub 3] Cathodes. J. Electrochem. Soc. 123, 960 (1976).
- Whittingham, M. S. Chemistry of intercalation compounds: Metal guests in chalcogenide hosts. Progress in Solid State Chemistry 12, (1978).
- 623 30. Holleck, G. L. & Driscoll, J. R. Transition metal sulfides as cathodes for secondary lithium batteries—II. titanium sulfides. *Electrochim.* 624 *Acta* 22, 647–655 (1977).
- 625 31. Whittingham, M. S. The Role of Ternary Phases in Cathode Reactions. J. Electrochem. Soc. 123, 315 (1976).
- 626 32. Lindic, M. H. *et al.* XPS investigations of TiOySz amorphous thin films used as positive electrode in lithium microbatteries. *Solid State Ionics* 176, 1529–1537 (2005).
- 33. Jacobson, A. J., Chianelli, R. R., Rich, S. M. & Whittingham, M. S. AMORPHOUS MOLYBDENUM TRISULFIDE: A NEW LITHIUM BATTERY CATHODE. Mat. Res. Bull 14, (1979).
- Doan-Nguyen, V. V. T. *et al.* Molybdenum Polysulfide Chalcogels as High-Capacity, Anion-Redox-Driven Electrode Materials for Li-Ion Batteries. *Chem. Mater* **28**, 42 (2016).
- Sakuda, A. *et al.* Amorphous Metal Polysulfides: Electrode Materials with Unique Insertion/Extraction Reactions. *J. Am. Chem. Soc.* **139**, 8796–8799 (2017).
- Britto, S. *et al.* Multiple Redox Modes in the Reversible Lithiation of High-Capacity, Peierls-Distorted Vanadium Sulfide. *J. Am. Chem. Soc* **137**, (2015).
- Butala, M. M. et al. Local Structure Evolution and Modes of Charge Storage in Secondary Li-FeS 2 Cells. Chem. Mater 29, (2017).
- Goodenough, J. B. & Kim, Y. Locating redox couples in the layered sulfides with application to Cu[Cr<sub>2</sub>]S<sub>4</sub>. J. Solid State Chem. **182**, 2904–2911 (2009).
- 639 39. Clark, S. J., Wang, D., Armstrong, A. R. & Bruce, P. G. Li(V0.5Ti0.5)S2 as a 1 V lithium intercalation electrode. *Nat. Commun.* 7, 10898 (2016).
- Tarascon, J. M., Disalvo, F. J., Eibschutz, M., Murphy, D. W. & Waszczak, J. V. Preparation and chemical and physical properties of the new layered phases LixTi1-yMyS2 with M=V,Cr,orFe. *Phys. Rev. B* **28**, 6397–6406 (1983).
- 41. Xie, Y., Saubanè, M. & Doublet, M. L. Requirements for reversible extra-capacity in Li-rich layered oxides for Li-ion batteries †. Energy Environ. Sci. 10, 266–274 (2017).
- 42. Li, B. *et al.* Thermodynamic Activation of Charge Transfer in Anionic Redox Process for Li-Ion Batteries. *Adv. Funct. Mater.* **28**, 1–11 (2018).
- 43. Lu, Z. & Dahn, J. R. Understanding the Anomalous Capacity of Li/Li[Ni<sub>x</sub>Li<sub>(1/3-2x/3)</sub>Mn<sub>(2/3-x/3)</sub>]O<sub>2</sub> Cells Using In Situ X-Ray Diffraction and Electrochemical Studies. *J. Electrochem. Soc.* **149**, A815 (2002).
- 44. Lu, Z., Beaulieu, L. Y., Donaberger, R. A., Thomas, C. L. & Dahn, J. R. Synthesis, Structure, and Electrochemical Behavior of Li[Ni<sub>x</sub>Li<sub>(1/3-2x/3)</sub>Mn<sub>(2/3-x/3)</sub>]O<sub>2</sub>. J. Electrochem. Soc. **149**, A778–A791 (2002).
- $\begin{array}{lll} \textbf{651} & \textbf{45.} & \text{Lu, Z., MacNeil, D. D. \& Dahn, J. R. Layered Cathode Materials Li} [Ni_x Li_{(1/3-2x/3)} Mn_{(2/3-x/3)}]O_2 \ \text{for Lithium-Ion Batteries.} \ \textit{Electrochem.} \\ \textbf{652} & \textit{Solid-State Lett. 4, A191 (2001).} \end{array}$
- 653 46. Flamary-Mespoulie, F. Synthèse et caractérisation de sulfures de métaux de transition comme matériaux d'électrode positive à forte capacité pour microbatteries au lithium, Université de Bordeaux. (2016).
- Shadike, *Z. et al.* Antisite occupation induced single anionic redox chemistry and structural stabilization of layered sodium chromium sulfide. *Nat. Commun.* **8**, 1–9 (2017).
- 48. Sakuda, A. et al. A Reversible Rocksalt to Amorphous Phase Transition Involving Anion Redox. Sci. Rep. 8, 15086 (2018).

- 658 49. Sakuda, A. et al. Rock-salt-type lithium metal sulphides as novel positive-electrode materials. Sci. Rep. 4, 2–6 (2014).
- 659 50. Matsunaga, T. et al. Dependence of Structural Defects in Li 2 MnO 3 on Synthesis Temperature. Chem. Mater. 28, 4143–4150 (2016).
- Furuseth, S., Brattås, L., Kjekshus, A., Andresen, A. F. & Fischer, P. On the Crystal Structures of TiS3, ZrS3, ZrSe3, ZrSe3, ZrTe3, HfS3, and HfSe3. *Acta Chem. Scand.* **29a**, 623–631 (1975).
- 662 52. Chamas, M., Sougrati, M.-T., Reibel, C. & Lippens, P.-E. Quantitative Analysis of the Initial Restructuring Step of Nanostructured FeSn 2 -Based Anodes for Li-Ion Batteries. *Chem. Mater.* 25, 2410–2420 (2013).
- Fatseas, G. A. & Goodenough, J. B. Mössbauer 57Fe spectra exhibiting "ferrous character". J. Solid State Chem. 33, 219–232 (1980).
- 54. Vaughan, D. J. & Ridout, M. S. Mössbauer studies of some sulphide minerals. J. Inorg. Nucl. Chem. 33, 741–746 (1971).
- Mchael Bancrofi, G., Kasrai, M., Fleet, M. & Stn, C. S K- AND L-EDGE X.RAY ABSORPTION SPECTROSCOPY OF METAL
  SULFIDES AND SULFATES: APPLICATIONS IN MINERALOGY AND GEOCHEMISTRY. Can. Mineral. 33, 949–960 (1995).
- 56. Fleet, M. E. XANES SPECTROSCOPY OF SULFUR IN EARTH MATERIALS. Can. Mineral. 43, 1811–1838 (2005).
- Kowalska, J. K. *et al.* Iron L2,3-Edge X-ray Absorption and X-ray Magnetic Circular Dichroism Studies of Molecular Iron Complexes with Relevance to the FeMoco and FeVco Active Sites of Nitrogenase. *Inorg. Chem.* **56**, 8147–8158 (2017).
- 58. Zhang, L. *et al.* Tracking the Chemical and Structural Evolution of the TiS2 Electrode in the Lithium-Ion Cell Using Operando X-ray Absorption Spectroscopy. *Nano Lett* **18**, 4506–4515 (2018).
- Farrell, S. P. *et al.* Evolution of local electronic structure in alabandite and niningerite solid solutions [(Mn,Fe)S, (Mg,Mn)S, (Mg,Fe)S] using sulfur K and L -edge XANES spectroscopy. *Am. Mineral.* 87, 1321–1332 (2002).
- 675 60. Yang, W. & Devereaux, T. P. Anionic and cationic redox and interfaces in batteries: Advances from soft X-ray absorption spectroscopy to resonant inelastic scattering. *J. Power Sources* **389**, 188–197 (2018).
- 677 61. Szilagyi, R. K. *et al.* Description of the Ground State Wave Functions of Ni Dithiolenes Using Sulfur K-edge X-ray Absorption Spectroscopy. *J. Am. Chem. Soc.* 125, 9158–9169 (2003).
- 679 62. Fleet, M. E., Harmer, S. L., Liu, X. & Nesbitt, H. W. Polarized X-ray absorption spectroscopy and XPS of TiS3: S K- and Ti L-edge XANES and S and Ti 2p XPS. *Surf. Sci.* **584**, 133–145 (2005).
- 681 63. Matsuyama, T. *et al.* Structure analyses using X-ray photoelectron spectroscopy and X-ray absorption near edge structure for amorphous MS3(M: Ti, Mo) electrodes in all-solid-state lithium batteries. *J. Power Sources* 313, 104–111 (2016).
- 683 64. Martinez, H. *et al.* Influence of the cation nature of high sulfur content oxysulfide thin films MO y S z (M½W, Ti) studied by XPS. *Appl. Surf. Sci.* 236, 377–386 (2004).
- 685 65. Strehle, B. *et al.* The Role of Oxygen Release from Li- and Mn-Rich Layered Oxides during the First Cycles Investigated by On-Line Electrochemical Mass Spectrometry. *J. Electrochem. Soc.* **164**, A400–A406 (2017).
- 687 66. Boultif, A. & Louer, D. Indexing of powder diffraction patterns for low-symmetry lattices by the successive dichotomy method. *J. Appl. Cryst.* 24, 987–993 (1991).
- 689 67. Rodríguez-Carvajal, J. FullProf Suite; all the programs can be obtained from: http://www.ill.eu/sites/fullprof.
- 690 68. Fehse, M. *et al.* The Electrochemical Sodiation of FeSb 2: New Insights from Operando <sup>57</sup> Fe Synchrotron Mössbauer and X-Ray Absorption Spectroscopy. *Batter. Supercaps* 2, 66–73 (2019).
- 692 69. Qiao, R. *et al.* High-efficiency in situ resonant inelastic x-ray scattering (iRIXS) endstation at the Advanced Light Source. *Rev. Sci. Instrum.* 88, (2017).
- 694 70. Shirley, D. A. High-resolution X-Ray photoemission spectrum of the valence bands of gold. *Phys. Rev. B* 5, 4709–4714 (1972).
- 595 71. Scofield, J. H. Hartree-Slater subshell photoionization cross-sections at 1254 and 1487 eV. *J. Electron Spectros. Relat. Phenomena* 8, 129–137 (1976).
- Ping Ong, S. *et al.* Python Materials Genomics (pymatgen): A robust, open-source python library for materials analysis. *Comput. Mater. Sci.* 68, 314–319 (2013).
- Kresse, G. & Joubert, D. From ultrasoft pseudopotentials to the projector augmented-wave method. *Phys. Rev. B* **59**, 1758–1775 (1999).
- 700 74. Perdew, J. P., Burke, K. & Ernzerhof, M. Generalized Gradient Approximation Made Simple. *Phys. Rev. Lett.* 77, 3865–3868 (1996).

701 75. Grimme, S., Ehrlich, S. & Goerigk, L. Effect of the damping function in dispersion corrected density functional theory. *J. Comput. Chem.* 32, 1456–1465 (2011).

705

703 76. Dudarev, S. L., Botton, G. A., Savrasov, S. Y., Humphreys, C. J. & Sutton, A. P. Electron-energy-loss spectra and the structural stability of nickel oxide: An LSDA+U study. *Phys. Rev. B* 57, 1505–1509 (1998).